


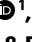



Rapid droplet-based mixing for single-molecule spectroscopy

Received: 27 February 2023

Accepted: 2 August 2023

Published online: 25 September 2023

 Check for updates

Tianjin Yang ¹✉, Karin J. Buholzer ¹, Andrea Sottini ¹, Xiaobao Cao², Andrew deMello², Daniel Nettels ¹ & Benjamin Schuler ^{1,3}✉

Probing non-equilibrium dynamics with single-molecule spectroscopy is important for dissecting biomolecular mechanisms. However, existing microfluidic rapid-mixing systems for this purpose are incompatible with surface-adhesive biomolecules, exhibit undesirable flow dispersion and are often demanding to fabricate. Here we introduce droplet-based microfluidic mixing for single-molecule spectroscopy to overcome these limitations in a wide range of applications. We demonstrate its robust functionality with binding kinetics of even very surface-adhesive proteins on the millisecond timescale.

Single-molecule spectroscopy has evolved into a versatile and widely used method for probing the nanoscale conformations, dynamics and conformational heterogeneity of biomolecules¹. In favorable cases, dynamics and kinetics can be monitored in equilibrium measurements, but probing non-equilibrium dynamics remains indispensable if the states and transitions of interest are not sampled at equilibrium². Examples include reactions that turn over a source of energy such as ATP; conformational transitions that are effectively irreversible, i.e. the forward and backward reactions occur on timescales that are too disparate to be observed simultaneously at equilibrium; or kinetics involving conformations whose populations are too small to be detectable at equilibrium. Correspondingly, microfluidic rapid-mixing systems have been developed to resolve fast biomolecular kinetics under non-equilibrium conditions with single-molecule spectroscopy. Although a wide range of active and passive microfluidic mixing methods are available³, hydrodynamic flow focusing has been the primary choice for interfacing with single-molecule spectroscopy^{4–10}. However, hydrodynamic flow-focusing devices have several limitations. First, many proteins strongly adsorb to solid–liquid interfaces, especially if they are marginally stable, hydrophobic or positively charged¹¹. The exceedingly large surface-area-to-volume ratios that are characteristic of microfluidic devices exacerbate adsorption and have prevented the use of hydrodynamic focusing for many biomolecular systems¹². Second, hydrodynamic focusing has often been implemented with very small structures of a few micrometers in width to enable rapid diffusive mixing in laminar flow. This necessitates microfabrication with an accuracy and precision that requires specialized equipment for deep reactive-ion etching in silicon and thus limits broad accessibility

of these important tools. Finally, Taylor dispersion¹³ in single-phase microfluidics introduces an intrinsic position-dependent uncertainty in the arrival times of molecules at the point of observation¹⁴, which complicates the quantitative analysis of kinetic measurements^{8,14}.

To overcome these limitations, we have developed a droplet-based microfluidic device for single-molecule spectroscopy. The design (Fig. 1a and Extended Data Fig. 1) enables rapid mixing within aqueous droplets formed in an oil phase, which act as picoliter containers that do not exchange components with the exterior as they travel through the device. Four inlets are used to deliver oil, buffer and the samples 1 and 2 to the primary microfluidic channel (Fig. 1a and Extended Data Figs. 1 and 2). The buffer solution sheathes sample 1, which prevents premature mixing with sample 2 and allows on-chip dilution. All liquids entering the microfluidic device pass through microfabricated inlet filters that prevent dust particles from clogging the device (Fig. 1a and Extended Data Fig. 1), which is essential for long-term flow stability (Extended Data Fig. 3). Droplets are formed by flow focusing¹⁵, in which part of the oil is branched off just before droplet formation and is recombined afterwards, accelerating the droplets into a serpentine channel that ensures sub-millisecond mixing inside the droplets by chaotic advection¹⁶. The non-ionic fluorosurfactant PEG-PFPE₂ in the oil phase is used to stabilize the droplets¹⁷ and prevent protein adhesion to the oil–water interface (Fig. 1d,e and Extended Data Fig. 6). The mixing time of small proteins in our measurements is 0.89 ± 0.03 ms, calibrated from the diffusion-limited quenching of fluorescein by potassium iodide (Extended Data Fig. 4 and Methods). After mixing, most of the oil is drained through two side channels to reduce the droplet velocity by two orders of magnitude and to reach passage

¹Department of Biochemistry, University of Zurich, Zurich, Switzerland. ²Institute for Chemical and Bioengineering, ETH Zurich, Zurich, Switzerland.

³Department of Physics, University of Zurich, Zurich, Switzerland. ✉ e-mail: t.yang@bioc.uzh.ch; schuler@bioc.uzh.ch

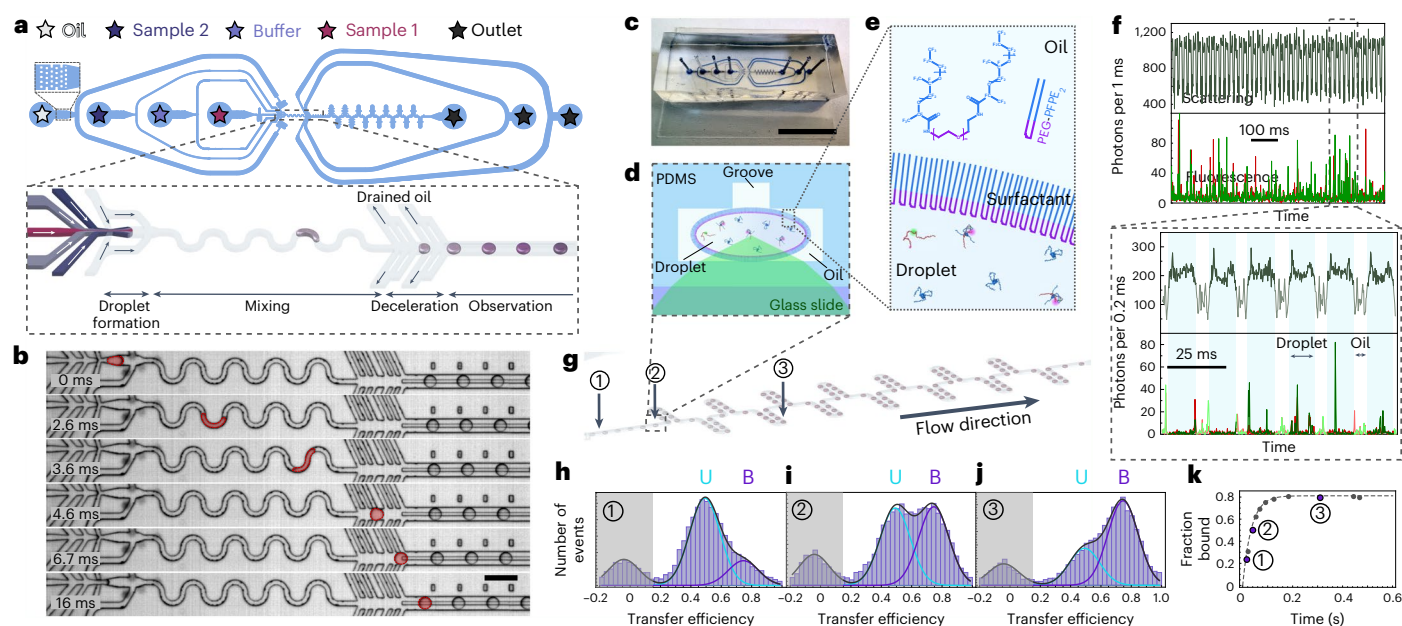


Fig. 1 | Design and operation of the droplet-based microfluidic mixer.

a, Schematic of the droplet-based microfluidic mixer. Spaced pillars in inlets (zoomed-in region) function as filters that prevent particles from entering the channels and blocking the device. The zoomed-in region depicts sample delivery, droplet formation, mixing (one droplet is shown), deceleration and droplets in the observation channel. **b**, The device in operation. A manually colored droplet at different time points indicates the changes in droplet velocity in different regions of the device. Scale bar, 100 μm . The representative snapshots are based on at least 50 independent repeats with similar results. **c**, The microfluidic device cast in PDMS. For visualization, the microchannels were filled with ink. Scale bar, 1 cm. **d**, Schematic cross-section of the observation channel, showing a perfluorosurfactant-stabilized droplet containing fluorophore-labeled protein molecules (not to scale) passing through the laser focus (excitation beam indicated in green). **e**, Zoom-in illustrating the droplet water–oil interface.

The non-ionic triblock copolymeric fluorosurfactant PEG-PFPE₂ stabilizes the droplets and prevents protein adhesion to the oil–water interface. The hydrophilic block is indicated in purple, and the hydrophobic blocks are shown in blue (not to scale). **f**, Light scattered by the droplets is detected simultaneously with fluorescence to identify individual droplets (blue shading), to determine droplet frequency and velocity and to eliminate the contribution of fluorescence from the oil phase. **g**, Measurements are performed at various positions (for example, 1, 2 and 3) along the observation channel. **h–j**, Examples of resulting FRET efficiency histograms showing the bound (purple fit line) and unbound populations (light-blue fit line) in a biomolecular binding reaction corresponding to different times after mixing as indicated in **k** (U, unbound; B, bound). The peak close to zero transfer efficiency (gray shading) originates from molecules without active acceptor dye. **k**, Resulting fractions of bound molecules as a function of time yield the reaction kinetics.

times through the confocal detection volume that are compatible with single-molecule fluorescence detection in the observation channel (Fig. 1a,b and Supplementary Video 1), resulting in a dead time of 4.8 ± 0.4 ms (Methods).

Notably, none of the feature sizes of the device are below 14 μm , which makes it compatible with simple microfabrication based on photoresists¹⁸ (Extended Data Fig. 5) and mask-free two-photon three-dimensional (3D) printing¹⁹. The devices were produced from the master by replica molding with polydimethylsiloxane (PDMS) (Fig. 1c and Extended Data Fig. 5)¹⁸, bonded to a glass cover slide coated with a thin layer of PDMS and mounted on a confocal single-molecule instrument, with the laser beam focused at the center of the droplets passing through the observation channel (Fig. 1d). Light scattering was detected simultaneously with the fluorescence signals to identify individual droplets in real time (Fig. 1f, shaded), determine droplet frequency and velocity and eliminate the contribution of fluorescence background from the oil phase (Methods and Extended Data Figs. 6 and 7). A groove on top of the observation channel (Fig. 1b,d and Extended Data Fig. 1a) stabilizes droplet position in the channel center during signal detection. To monitor the kinetics of a reaction, the confocal detection volume was moved to different positions along the observation channel, corresponding to different times after mixing, from a few milliseconds to 4 s (Fig. 1g). In the example in Fig. 1, donor and acceptor emission from molecules labeled for single-molecule Förster resonance energy transfer (FRET) was recorded. The resulting transfer efficiency histograms (Fig. 1h–j) yield the changes in molecular populations over time and can be analyzed kinetically (Fig. 1k).

To demonstrate the on-chip detection capability of single-molecule FRET in a fast biomolecular reaction on the millisecond time scale, we first investigated the coupled folding and binding of the intrinsically disordered activation domain of the p160 transcriptional coactivator (ACTR) and the nuclear coactivator binding domain (NCBD) of CREB-binding protein²⁰, essential regulators of eukaryotic transcription (Fig. 2a)²¹. A 50 pM solution of ACTR labeled with Cy3B and LD650 (ref. 22) as FRET donor and acceptor, respectively, was mixed with an excess of unlabeled NCBD to trigger complex formation (Fig. 2b), and transfer efficiency histograms were recorded at different times after mixing (Fig. 2c and Extended Data Fig. 8). To quantify the concentration dependence of this bimolecular reaction, the experiments were performed with NCBD concentrations between 25 and 150 nM. A global analysis of all data sets (Fig. 2d) yielded a dissociation rate constant, k_{off} , of 13.1 ± 0.6 s⁻¹, an association rate constant, k_{on} , of 0.74 ± 0.02 nM⁻¹ s⁻¹ and an equilibrium dissociation constant, K_{D} , of 17.7 ± 0.9 nM (calculated from k_{off} and k_{on}), in agreement with previous results^{10,23}. However, in measurements using hydrodynamic focusing¹⁰, surface adsorption of NCBD necessitated independent knowledge of K_{D} to determine k_{on} and k_{off} , in contrast to our droplet-based microfluidic system, which prevents surface adsorption.

An even more demanding test of the droplet-based mixing device is the binding reaction between two highly and oppositely charged IDPs, whose severe surface adhesion has prevented any measurements in microfluidic devices. The human proteins prothymosin α (ProT α , net charge -44) and linker histone H1.0 (H1, net charge +53) (Fig. 2e) interact with picomolar to nanomolar affinity at physiological salt

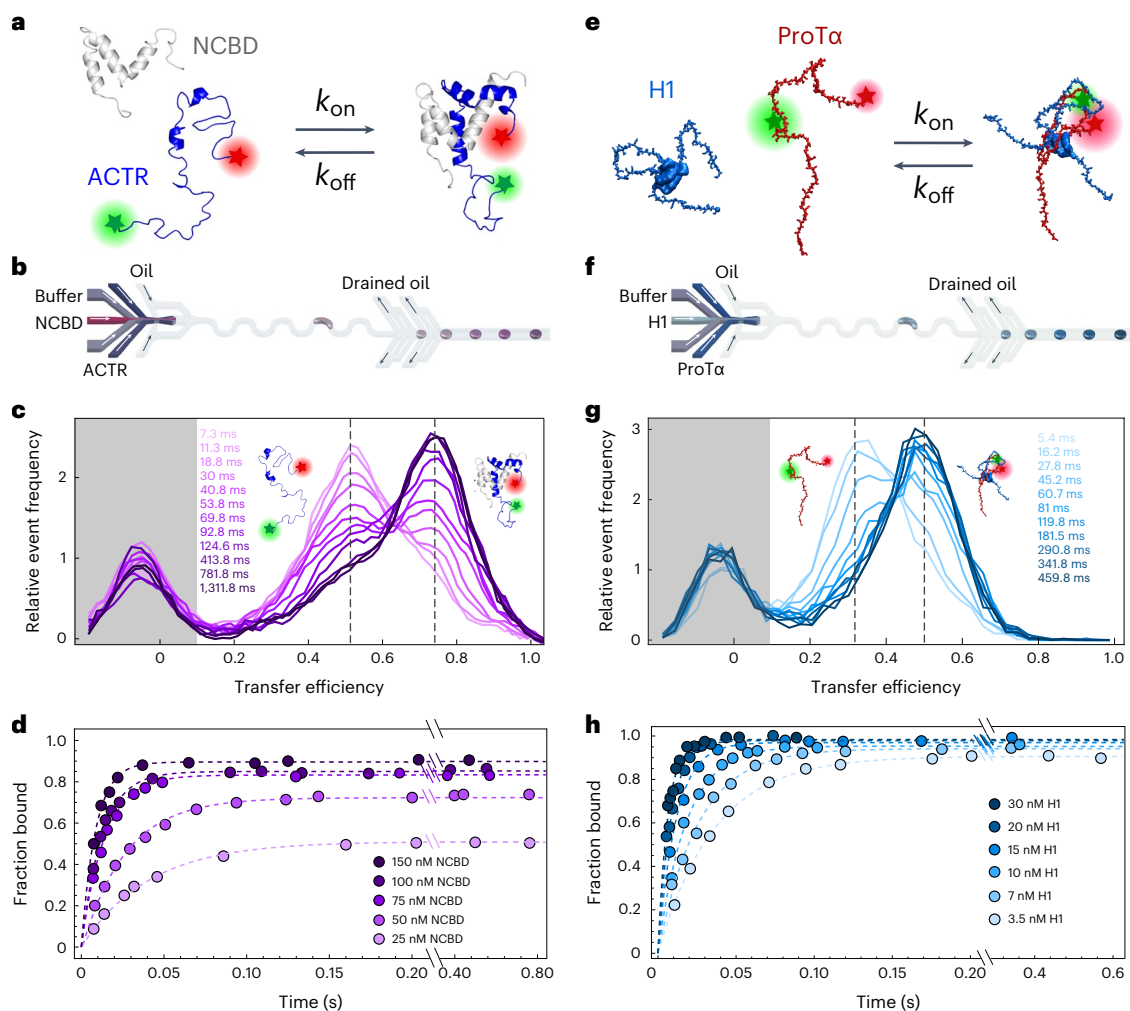


Fig. 2 | Droplet-based mixing enables the detection of rapid binding kinetics.

a, Illustration of the coupled folding and binding of the intrinsically disordered proteins ACTR and NCBD. **b**, Donor- and acceptor-labeled ACTR was mixed with an excess of unlabeled NCBD to trigger complex formation. **c**, Normalized histograms of transfer efficiency (E) measured at different positions along the observation channel after mixing in droplets containing 50 pM ACTR and 50 nM NCBD, corresponding to different times after the start of the reaction. The low transfer efficiency peak at $\langle E \rangle \approx 0.51$ corresponds to free, disordered ACTR; the high transfer efficiency peak at $\langle E \rangle \approx 0.74$ corresponds to folded ACTR in complex with NCBD. **d**, Global fit (dashed colored lines) of the association kinetics for five NCBD concentrations (25, 50, 75, 100 and 150 nM) yielded a k_{off} of $13.1 \pm 0.6 \text{ s}^{-1}$, a

k_{on} of $0.74 \pm 0.02 \text{ nM}^{-1} \text{ s}^{-1}$ and a K_{D} of $17.7 \pm 0.9 \text{ nM}$. **e**, Illustration of the binding of the highly charged, disordered proteins ProT α and H1. **f**, Donor- and acceptor-labeled ProT α was mixed with an excess of unlabeled H1 to trigger complex formation. **g**, Normalized transfer efficiency histograms measured at various positions along the channels after mixing in droplets containing 50 pM ProT α and 7 nM H1 (ionic strength 200 mM), corresponding to different times after the start of the reaction. The low transfer efficiency peak at $\langle E \rangle \approx 0.33$ corresponds to free ProT α ; the high transfer efficiency peak at $\langle E \rangle \approx 0.51$ corresponds to the ProT α –H1 complex. **h**, Global fit (dashed colored lines) of the association kinetics for six different H1 concentrations (3.5, 7, 10, 15, 20 and 30 nM) yielded $k_{\text{off}} = 2.9 \pm 0.3 \text{ s}^{-1}$, $k_{\text{on}} = 5.8 \pm 0.2 \text{ nM}^{-1} \text{ s}^{-1}$ and $K_{\text{D}} = 0.50 \pm 0.05 \text{ nM}$.

concentrations but retain their disorder in the bound state²⁴. The pronounced stickiness of H1 poses a particular challenge, even in equilibrium single-molecule measurements²⁴. We mixed ProT α labeled with Alexa Fluor 488 and Alexa Fluor 594 with unlabeled H1 (Fig. 2f), and recorded transfer efficiency histograms (Fig. 2g and Extended Data Fig. 9) to monitor the kinetics of complex formation. H1 binding causes an increase in transfer efficiency because the mutual charge screening of the oppositely charged IDPs leads to ProT α compaction²⁴. With a dead time of $4.8 \pm 0.4 \text{ ms}$, the device reaches its limits for observed rates above $\sim 150 \text{ s}^{-1}$. To enable reliable measurements at H1 concentrations above 30 nM, we produced a mixing device with scaled-down channel sizes, which is slightly more challenging to handle, but reduces the dead time to $1.7 \pm 0.3 \text{ ms}$ (Methods, Extended Data Fig. 10a and Supplementary Video 2). The consistency of the results for the two device sizes (Extended Data Fig. 10b) demonstrates the robustness of the overall design and shows that the channel dimensions can be adjusted

to optimize the dead time and temporal resolution required for a desired application. A global analysis of all kinetic data for ProT α –H1 binding (Fig. 2h) yielded values of $k_{\text{on}} = 5.8 \pm 0.2 \text{ nM}^{-1} \text{ s}^{-1}$, $k_{\text{off}} = 2.9 \pm 0.3 \text{ s}^{-1}$ and $K_{\text{D}} = 0.50 \pm 0.05 \text{ nM}$ (calculated from k_{off} and k_{on}), consistent with equilibrium measurements²⁵.

Our results thus establish the feasibility of single-molecule FRET measurements in droplet-based microfluidics. We show that they enable rapid mixing with millisecond dead times and overcome several limitations. Most importantly, they enable non-equilibrium kinetic measurements with samples whose pronounced surface adhesion or sensitivity to interfaces has previously precluded such investigations. Important examples are positively charged IDPs or large biomolecular assemblies. The droplets represent individual picoliter containers lined with the non-ionic fluorosurfactant PEG-PFPE₂, so surface adhesion of biomolecules both to the channel walls and the oil–water interface is minimized. Moreover, the position-to-time conversion

of measurements along the observation channel is simple, given the known droplet velocity and the absence of Taylor dispersion¹⁴, which is unavoidable in single-phase designs. Finally, in contrast to many established single-molecule microfluidic mixing devices, fabrication is possible in photoresists such as SU-8, which will ensure broad applicability without access to specialized microfabrication facilities. Our simple but robust and versatile system allows single-molecule FRET kinetics to be probed under non-equilibrium conditions in a tether-free fashion from milliseconds to seconds. Droplet frequencies and flow velocities can be precisely tuned and directly obtained during the measurements without demanding flow calculations¹⁴. These results set the stage for the broad use of droplet-based microfluidic devices with single-molecule detection. A limitation of the current design is the maximum observation time of a few seconds. However, since the droplets serve as individual reaction containers, the observation time could be extended with a longer observation channel or storage array²⁶. Other promising future developments include combining the design with advanced detection modalities²⁶ such as three-color FRET⁹, and incorporating temperature control^{8,27} and rapid laser-based triggering techniques or the downstream addition of reagents by picoinjection²⁸ for monitoring multi-step reactions.

Online content

Any methods, additional references, Nature Portfolio reporting summaries, source data, extended data, supplementary information, acknowledgements, peer review information; details of author contributions and competing interests; and statements of data and code availability are available at <https://doi.org/10.1038/s41592-023-01995-9>.

References

- Lerner, E. et al. Toward dynamic structural biology: two decades of single-molecule Förster resonance energy transfer. *Science* **359**, eaan1133 (2018).
- Schuler, B. Single-molecule FRET of protein structure and dynamics—a primer. *J. Nanobiotechnology* **11**, S2 (2013).
- Capretto, L., Cheng, W., Hill, M. & Zhang, X. Micromixing within microfluidic devices. *Top. Curr. Chem.* **304**, 27–68 (2011).
- Knight, J. B., Vishwanath, A., Brody, J. P. & Austin, R. H. Hydrodynamic focusing on a silicon chip: mixing nanoliters in microseconds. *Phys. Rev. Lett.* **80**, 3863–3866 (1998).
- Lipman, E. A., Schuler, B., Bakajin, O. & Eaton, W. A. Single-molecule measurement of protein folding kinetics. *Science* **301**, 1233–1235 (2003).
- Pfeil, S. H., Wickersham, C. E., Hoffmann, A. & Lipman, E. A. A microfluidic mixing system for single-molecule measurements. *Rev. Sci. Instrum.* **80**, 055105 (2009).
- Gambin, Y. et al. Visualizing a one-way protein encounter complex by ultrafast single-molecule mixing. *Nat. Methods* **8**, 239–241 (2011).
- Wunderlich, B. et al. Microfluidic mixer designed for performing single-molecule kinetics with confocal detection on timescales from milliseconds to minutes. *Nat. Protoc.* **8**, 1459–1474 (2013).
- Zijlstra, N. et al. Rapid microfluidic dilution for single-molecule spectroscopy of low-affinity biomolecular complexes. *Angew. Chem. Int. Ed.* **56**, 7126–7129 (2017).
- Dingfelder, F. et al. Rapid microfluidic double-jump mixing device for single-molecule spectroscopy. *J. Am. Chem. Soc.* **139**, 6062–6065 (2017).
- Vogler, E. A. Protein adsorption in three dimensions. *Biomaterials* **33**, 1201–1237 (2012).
- Zhang, H. & Chiao, M. Anti-fouling coatings of poly(dimethylsiloxane) devices for biological and biomedical applications. *J. Med. Biol. Eng.* **35**, 143–155 (2015).
- Taylor, G. I. Dispersion of soluble matter in solvent flowing slowly through a tube. *Proc. R. Soc. Lond. A* **219**, 186–203 (1953).
- Wunderlich, B., Nettels, D. & Schuler, B. Taylor dispersion and the position-to-time conversion in microfluidic mixing devices. *Lab Chip* **14**, 219–228 (2014).
- Anna, S. L., Bontoux, N. & Stone, H. A. Formation of dispersions using ‘flow focusing’ in microchannels. *Appl. Phys. Lett.* **82**, 364–366 (2003).
- Song, H., Bringer, M. R., Tice, J. D., Gerds, C. J. & Ismagilov, R. F. Experimental test of scaling of mixing by chaotic advection in droplets moving through microfluidic channels. *Appl. Phys. Lett.* **83**, 4664–4666 (2003).
- Baret, J.-C. Surfactants in droplet-based microfluidics. *Lab Chip* **12**, 422–433 (2012).
- Qin, D., Xia, Y. & Whitesides, G. M. Soft lithography for micro- and nanoscale patterning. *Nat. Protoc.* **5**, 491–502 (2010).
- Harinarayana, V. & Shin, Y. C. Two-photon lithography for three-dimensional fabrication in micro/nanoscale regime: a comprehensive review. *Opt. Laser Technol.* **142**, 107180 (2021).
- Dogan, J., Schmidt, T., Mu, X., Engström, Å. & Jemth, P. Fast association and slow transitions in the interaction between two intrinsically disordered protein domains. *J. Biol. Chem.* **287**, 34316–34324 (2012).
- Dyson, H. J. & Wright, P. E. Role of intrinsic protein disorder in the function and interactions of the transcriptional coactivators CREB-binding protein (CBP) and p300. *J. Biol. Chem.* **291**, 6714–6722 (2016).
- Altman, R. B. et al. Cyanine fluorophore derivatives with enhanced photostability. *Nat. Methods* **9**, 68–71 (2011).
- Dogan, J., Jonasson, J., Andersson, E. & Jemth, P. Binding rate constants reveal distinct features of disordered protein domains. *Biochemistry* **54**, 4741–4750 (2015).
- Borgia, A. et al. Extreme disorder in an ultrahigh-affinity protein complex. *Nature* **555**, 61–66 (2018).
- Sottini, A. et al. Polyelectrolyte interactions enable rapid association and dissociation in high-affinity disordered protein complexes. *Nat. Commun.* **11**, 5736 (2020).
- Charmet, J., Arosio, P. & Knowles, T. P. J. Microfluidics for protein biophysics. *J. Mol. Biol.* **430**, 565–580 (2018).
- Yang, T. et al. Droplet-based microfluidic temperature-jump platform for the rapid assessment of biomolecular kinetics. *Anal. Chem.* **94**, 16675–16684 (2022).
- Abate, A. R., Hung, T., Mary, P., Agresti, J. J. & Weitz, D. A. High-throughput injection with microfluidics using picoinjectors. *Proc. Natl Acad. Sci. USA* **107**, 19163–19166 (2010).

Publisher’s note Springer Nature remains neutral with regard to jurisdictional claims in published maps and institutional affiliations.

Springer Nature or its licensor (e.g. a society or other partner) holds exclusive rights to this article under a publishing agreement with the author(s) or other rightsholder(s); author self-archiving of the accepted manuscript version of this article is solely governed by the terms of such publishing agreement and applicable law.

© The Author(s), under exclusive licence to Springer Nature America, Inc. 2023

Methods

Microfluidic device fabrication

Masters for casting the standard-scale microfluidic mixer (Extended Data Fig. 1a) were fabricated using two alternative approaches: conventional photolithography¹⁸ and mask-free two-photon 3D printing¹⁹. When using conventional lithography (Extended Data Fig. 5), microfluidic structures were designed using AutoCAD 2019 (Autodesk). Photomasks for the two layers of the device, the main channel system (see mask layout) and the groove channel for droplet alignment in the observation channel (see mask layout), were printed separately on high-resolution film (Micro Lithography Services). SU-8 2015 photoresist (MicroChemicals) was deposited on silicon wafers (diameter 100 mm ± 0.2, thickness 500 ± 25 μm, surface polished, Applied Materials) by spin coating at 2,200 r.p.m. to achieve a film thickness of 20 μm. The wafer was soft-baked on a hot plate for 3 min at 95 °C and then exposed to UV light (energy density: 140 mJ cm⁻² at 365 nm), with the main channel mask aligned 20 μm above the wafer (mask aligner MA6/MB6, Süss). Next, the wafer was placed on a hot plate for 3 min at 95 °C for the post-exposure bake. A layer of SU-8 2007 (MicroChemicals) was spin-coated on the previous layer at 1,500 r.p.m. to achieve a thickness of 10 μm and was soft-baked for 1 min at 65 °C, followed by 2 min at 95 °C. Utilizing the mask aligner, the groove channel photomask was aligned with the exposed structure on the wafer, and another UV exposure (energy density: 120 mJ cm⁻² at 365 nm) was used to create the groove channel. After post-exposure baking for 3 min at 95 °C, non-crosslinked photoresist was removed by gently shaking the wafer in SU-8 developer (MicroChemicals). The height of the microchannels was 20.0 ± 0.8 μm, with a 10.0 ± 0.5 μm deep groove along the observation channel (Fig. 1d). The channel widths were 14.0 ± 0.2 μm for the flow focusing channel, 55.0 ± 0.3 μm for the observation channel and 20.0 ± 0.2 μm for the serpentine channel for rapid mixing, as characterized by non-contact 3D laser scanning (Keyence VR-5000, Keyence).

For mask-free two-photon 3D printing, master structures were fabricated on a silicon wafer using a femtosecond laser lithography system (Photonic Professional GT, Nanoscribe). In the printing process, the laser is used to expose a negative-tone resin (IP-S, Nanoscribe) by means of a high-numerical aperture objective to achieve layer-by-layer two-photon polymerization. The material polymerizes only in the region of the laser focus, allowing the additive build-up of 3D structures. Writing parameters for slicing and hatching distances were set to 0.2 and 0.3 μm, respectively. After printing, the device was washed with isopropanol to remove residual photoresist. The height of the microchannels was 20 μm, the height of the groove was 10 μm, the width of the observation channel was 55 μm and the width of the serpentine channel for rapid mixing was 20 μm, as characterized by the Keyence 3D laser scanner. The precision of two-photon 3D printing is sufficient for structures in this size range but is insufficient for the reliable production of rapid-mixing devices on the basis of flow focusing that require a precision in the range of 0.1 μm (refs. 8,10,29).

The master of the scaled-down microfluidic mixer (Extended Data Fig. 1b) was fabricated on SU-8-2015-coated silicon wafers, following the same procedures as for the standard-scale device. After spin coating at 4,000 r.p.m., the wafer was soft-baked on a hot plate for 3 min at 95 °C and exposed to UV light with the photomask aligned 20 μm above the wafer (energy density: 140 mJ cm⁻² at 365 nm). Then the wafer was placed on a hot plate for 3 min at 95 °C for post-exposure baking. Non-crosslinked photoresist was removed by gently shaking the wafer in SU-8 developer for 3 min. The height of the microchannels was 12.0 ± 0.4 μm, and the widths were 6.0 ± 0.2 μm for the flow-focusing channel, 20 ± 0.2 μm for the observation channel and 12 ± 0.2 μm for the serpentine channel for rapid mixing, as characterized by 3D laser scanning (Keyence VR-5000, Keyence). Prior to replica molding, the masters were silanized with chlorotrimethylsilane (TMCS, Sigma-Aldrich) in a desiccator for 1 h to prevent PDMS adhesion.

Microfluidic devices were manufactured using replica molding¹⁸ (Extended Data Fig. 5). Briefly, a 10:1 wt/wt mixture of polydimethylsiloxane (PDMS) base and curing agent (RTV 615, Momentive Performance Materials) was poured onto the master structure in a petri dish and was then degassed and cured at 70 °C for 4 h. The cured PDMS structure (~0.5 cm thick) was peeled off the wafer and diced, and inlet and outlet ports were introduced using a hole puncher (diameter 0.9 mm, inside cutting edge, SYNEO). A 23 mm × 30 mm glass cover slide (NO.1, Esco Optics) was first cleaned by boiling with 2% deconex (INSTRUMENT PLUS, Borer Chemie) solution and double-distilled water, air dried and then spin-coated with a thin layer of PDMS (spin coating at 4,000 r.p.m., ~20-μm thickness) as the bottom layer. The structured and the bottom layers were bonded after plasma activation (Femto 1 A, Diener Electronic) for 60 s at 25% power. To prevent wetting of the microchannel surfaces by the water phase (for generating stable and homogeneous-size droplets), microfluidic channels were filled with a 5% (by volume) solution of 1*H*,1*H*,2*H*,2*H*-perfluorooctyltrichlorosilane (PFOCTS, ABCR-chemicals) in isopropanol for 3 min at room temperature (directly after plasma bonding) and then placed on a hot plate at 120 °C for 2 h. In addition, the PFOCTS monolayer reduces protein adhesion to the channel surface before the formation of droplets.

Microfluidic device operation

Four precision pressure-based flow controllers (Lineup Flow EZ 2,000 mbar, Fluigent) supplied with pressurized air at 2 bar were used for accurate control of fluid flow (Extended Data Fig. 2). Three of the pressure pumps were connected to individual flow sensors (Flow Unit XS, Fluigent) to deliver the aqueous phase to sample inlet 1, buffer inlet and sample inlet 2, with defined flow rates for achieving the target concentrations. The three pressure pumps delivering the aqueous phase were connected through tubing with a 5/32 in. outer diameter (OD) and 3/32 in. inner diameter (ID) to air-tight metal caps (P-CAP, Fluigent) sealed on 2-ml Eppendorf tubes containing double-distilled water, which served as reservoirs. Polyether ether ketone (PEEK) tubing (1/32 in. OD, 0.01 in. ID) was used to connect the water reservoirs to the inlets of the flow sensors. The use of double-distilled water and particle filters (mesh size 2 μm) prevents clogging of the XS flow sensors. The flow sensor's outlet PEEK tubing (1/32 in. OD, 0.01 in. ID) was connected to PTFE tubing (1/16 in. OD), in which the sample and buffer solutions were stored, and which was connected to the inlets of the microfluidic device. We avoided running sample and buffer solutions through the flow sensor and instead stored sample and buffer solutions in this part of the tubing owing to a high risk of the flow sensor becoming clogged by dust particles, salt precipitates or biomolecular aggregates, given the small internal-channel diameter (20 μm). Owing to the large length-to-diameter ratio of the tubing and the slow flow through the tubing, the dilution of the sample introduced to the microfluidic chip is negligible. The fourth flow controller, coupled to a flow sensor (Flow Unit M, Fluigent), was connected via tubing (5/32 in. OD, 3/32 in. ID) to an air-tight P-CAP sealed on a 15-ml Falcon tube containing the oil. PEEK tubing (1/32 in. OD, 0.01 in. ID) was used to connect the oil reservoir to the inlet and outlet of the flow sensors. PTFE tubing (1/16 in. OD, 1/32 in. ID) was used to connect the outlet of the flow sensor to the microfluidic oil inlet through an adapter. The outlets of the microfluidic chip were connected to the waste reservoir through PTFE tubing (1/16 in. OD). All tubing was purchased from Fluigent. Pressures and flow rates of the four inlets were controlled and recorded every 20 ms during the experiment using the Fluigent A-i-O software. Owing to the narrow flow-focusing channel of the small device, channel blockage was more frequent than in the standard-scale device, making handling more difficult.

HFE-7500 oil (3M) containing 1% (wt/wt) of the non-ionic tri-block copolymer fluorosurfactant PEG-PFPE₂ (RAN Biotechnologies) was used as the carrier phase for all experiments (Fig. 1e). Typically, the

flow rate of the continuous phase was set to $10 \mu\text{L min}^{-1}$, and the flow rate of the aqueous phases was set to 20 nL min^{-1} for measurements (Supplementary Video 1, recorded at $3,000 \text{ frames s}^{-1}$, played at 40 frames s^{-1}). For the measurements performed in the small-scale device, the flow rate of the oil phase was set to $6 \mu\text{L min}^{-1}$, and the flow rate of the aqueous phases was set to 10 nL min^{-1} (Supplementary Video 2, recorded at $3,000 \text{ frames s}^{-1}$, played at 40 frames s^{-1}). The surfactant is crucial for producing stable droplets of well-defined size¹⁷. Furthermore, its biocompatibility and non-ionic nature prevent protein adsorption at the droplet–oil interface (Fig. 1d,e and Extended Data Fig. 6). When the surfactant concentration is too low in the oil phase, Cy3B- or LD650-labeled ACTR adsorbed at the oil–water interface (Extended Data Fig. 6a). By increasing the surfactant concentration to 1% (Extended Data Fig. 6b), adsorption was prevented (also for Alexa-Fluor-488- and Alexa-Fluor-594-labeled ProTx, Extended Data Fig. 6c). The fluorosurfactant increases background fluorescence in the oil phase (Extended Data Fig. 6d), but not inside the droplets. The selective fluorescence analysis described below enabled single-molecule spectroscopy.

Droplet velocity and mixing-time calibration

Mixing times in the microfluidic device were quantified by monitoring fluorescein quenching by iodide. The three inlets were supplied with a $60 \mu\text{M}$ fluorescein solution (fluorescein sodium, Fluka, Buchs, Switzerland) in 0.1 M NaOH (Sigma-Aldrich), pure 0.1 M NaOH solution and 1.8 M potassium iodide (Sigma-Aldrich), respectively, at equal flow rates (Extended Data Fig. 4a). Flow rates could be adjusted to achieve different droplet velocities. The droplet velocity in the mixing channel was measured via bright-field imaging with a high-speed camera (EoSens 4 CXP, MIKROTRON) on an inverted microscope (IX71 Olympus). The active area of the camera was set to $2,336 \times 300$ pixels, with a framerate of 3 kHz , to monitor droplet formation, droplet size and the position of individual droplets along the channel (Extended Data Fig. 4b). From the time between frames and the known lengths of the microfluidic channels, droplet velocities were calculated.

Wide-field fluorescence imaging was performed on the same microscope equipped with a 488-nm solid-state laser (Sapphire 488–100, Coherent). The laser light was focused onto the back aperture of a microscope objective (Plan, 20x, numerical aperture (NA) 0.40, Olympus) using a dichroic mirror (488 nm , Semrock). After passing through an emission bandpass filter (Brightline HQ525/50, Chroma), fluorescence was imaged on an sCMOS camera (Sona 4.2B-II, Andor Technology). For the rapidly moving droplets in the mixing channel, the exposure was set to 3 s . Ten frames were recorded to collect signal from at least $1,200$ droplets (Extended Data Fig. 4c).

A flat-field correction was applied to the fluorescence images, I_{raw} , to eliminate artifacts caused by uneven illumination. Reference images, I_{ref} , were recorded with fluorescein of known concentration in the absence of quencher but under identical flow and exposure conditions. The measured signal was corrected using:

$$I = \frac{I_{\text{raw}} - I_{\text{dc}}}{I_{\text{ref}} - I_{\text{dc}}} \quad (1)$$

where I_{dc} is a dark count image of the camera recorded with the camera shutter closed. The reference dye solution contained $5 \mu\text{M}$ fluorescein, pH 10. All measurements were performed under conditions that avoid saturation effects. From the averaged and flat-field-corrected fluorescence images, fluorescence intensities were read at multiple positions along the center of the mixing channel (Extended Data Fig. 4c). From these values, the normalized fluorescence intensity as a function of time was obtained for various droplet velocities (from 19.3 to 62.2 cm s^{-1}) (Extended Data Fig. 4d). The droplet size was identical under all conditions used here (the length of the droplet was $\sim 90 \mu\text{m}$ in the

mixing channel). We fitted the kinetic curves with a sigmoidal function $f_m(t)$ (Extended Data Fig. 4d):

$$f_m(t) = 1 - \frac{t^n}{c + t^n} \quad (2)$$

where t is the reaction time, and c and n are fit parameters. The mixing times (t_{mix} , defined as 90% of the extent of fluorescence intensity change) at different droplet velocities were obtained from the fit and plotted according to¹⁶:

$$t_{\text{mix}} \propto a \frac{w}{U} \log(\text{Pe}), \text{ Pe} = w \times U/D, \quad (3)$$

(Extended Data Fig. 4e), where $w = 20 \mu\text{m}$ is the width of the channel, a is the ratio of droplet length ($l = 90 \mu\text{m}$) over w and U is the velocity of the droplet. We used $D = 2.05 \times 10^{-9} \text{ m}^2 \text{ s}^{-1}$, the diffusion coefficient of iodide³⁰, because its value is much greater than that of fluorescein. Pe is the Peclet number, which indicates the ratio of the rate of advection to the rate of diffusion of the fluid. The mixing times are proportional to $w/U \times \log(\text{Pe})$ (Extended Data Fig. 4e), as predicted by Eq. (3). The linear fit of the plot is used as a calibration curve to determine the mixing time on the basis of the droplet velocities and the diffusion coefficients of the components in single-molecule FRET measurements. We assumed a diffusion coefficient of $10^{-10} \text{ m}^2 \text{ s}^{-1}$ for a small protein, and the droplet size was kept the same as in the mixing calibration (the length of the droplet was $90 \mu\text{m}$ in the mixing channel). The linear relation in Extended Data Fig. 4e then results in a mixing time of $0.89 \pm 0.03 \text{ ms}$ with a droplet velocity of 46.2 cm s^{-1} during mixing, the conditions used for the single-molecule FRET measurements. The influence of the diffusion coefficient on the mixing time is relatively weak owing to the logarithmic dependence in Eq. (3). For instance, using the diffusion coefficients of NCBD ($1.3 \times 10^{-10} \text{ m}^2 \text{ s}^{-1}$)³¹ and ProTx ($5.5 \times 10^{-11} \text{ m}^2 \text{ s}^{-1}$)²⁴ yields mixing times of $0.87 \pm 0.03 \text{ ms}$ and $0.92 \pm 0.03 \text{ ms}$, respectively. Accordingly, effects from the typical differences between the diffusion coefficients of small proteins on their mixing times are negligible. ImageJ (1.52f, National Institutes of Health) was used for image processing.

Position-to-time conversion and stability of the microfluidic system

To convert the detection position along the observation channel to the time after the start of the reaction, the dead time of the system and the residence time of the droplets at each detection position after they enter the observation channel must be known. The dead time of the device was defined as the interval between the time when mixing is 90% complete and the time when the droplet enters the observation channel. The time that the droplet travels in the mixing channel, $t_m = 3.0 \pm 0.3 \text{ ms}$, and the time of droplet deceleration up to the observation channel, $t_d = 2.7 \pm 0.3 \text{ ms}$ (Fig. 1a), were determined by bright-field imaging with the high-speed camera. $t_{\text{mix}} = 0.89 \pm 0.03 \text{ ms}$ was obtained from the calibration (Extended Data Fig. 4e) for the observed velocity of the droplet during mixing and adjusted for the diffusion coefficient of a small protein on the basis of Eq. (3). The dead time was then calculated using:

$$t_{\text{dead}} = t_m + t_d - t_{\text{mix}}, \quad (4)$$

resulting in a value of $4.8 \pm 0.4 \text{ ms}$. The temporal resolution of the device is essentially determined by the transit time of a droplet passing the focus, resulting in a value of approximately $\pm 5 \text{ ms}$ based on the droplet velocity and radius used. From the same considerations for the small-scale mixing device, we obtained a dead time of $1.7 \pm 0.3 \text{ ms}$ and a temporal resolution of approximately $\pm 2 \text{ ms}$. In both cases, dead time and temporal resolution are thus coordinated to be in a similar range. Notably, the temporal resolution in droplet-based microfluidics is

constant along the observation channel. This is in contrast to microfluidic mixing devices based on hydrodynamic focusing, in which the absolute temporal resolution decreases monotonically along the observation channel because of Taylor dispersion¹⁴. The length of the mixing channel was chosen to allow the device to be used broadly, including solutions with higher viscosity or with large biomolecules or complexes with a small diffusion coefficient (down to $\sim 10^{-14}$ m² s⁻¹, for example nucleosomes or ribosomes).

During single-molecule FRET measurements, besides donor and acceptor fluorescence, we recorded in parallel light scattering from the droplet–oil interfaces. The scattering signal allows us to monitor the droplet velocity and identify the time intervals during which a droplet passes the confocal volume. In this way, we can exclude fluorescence background emitted from the oil phase from analysis (see Fig. 1f). From the average passage time (11 ± 1 ms) and droplet diameter (50 ± 0.6 μ m) in the observation channel (averaged over tens of thousands of droplets observed with the high-speed camera), the droplet velocity was calculated as 4.6 ± 0.2 mm s⁻¹. In experiments with excitation at 488 nm, the fluorescence background signal from the oil phase is higher than the signal in the droplets (Extended Data Figs. 6c and 7). We thus identified the two phases directly from the donor and acceptor time traces (Extended Data Fig. 7).

The flow rates and droplet-generation frequencies of the microfluidic mixer remain stable for hours to days if sufficient sample volumes are provided. For two representative measurements of ACTR–NCBD (Fig. 2a–d) and H1–Pro α (Fig. 2e–h) association kinetics, the droplet velocities at different positions along the observation channel (plotted as a function of reaction time in Extended Data Fig. 3a,b) are stable, illustrating the long-term stability of the microfluidic mixer during hours of signal acquisition. Droplet velocities very close to the entrance of the observation channel (10 μ m from the entrance) are slightly higher, since droplet deceleration is not yet complete. Droplet frequencies at different positions along the observation channel (Extended Data Fig. 3c), based on the measurements in Extended Data Fig. 3b, illustrate the long-term stability of droplet formation in the system.

ACTR and NCBD expression, purification and labeling

For ACTR, the coding sequence was cloned into a pAT222–pD expression vector (gift of J. Schöppe and A. Plückthun)³² via BamHI/HindIII cloning sites. This yielded an expression construct of ACTR with two terminal Cys residues, an amino-terminal Avi-tag and a thrombin-cleavable carboxy-terminal His₆ tag: MAGLNIDIFEAQKIEWHEGSMGSGSPCGTQNRPLLRNSLDDLVLGPPSNLEGQSDERALLDQLHTLLSNTDATGLEEIDRALGIPELVNQQALEPKQDCGGPRGSRSQASHHHHHH. For *in vivo* biotinylation of Lys12 in the Avi-tag, pBirAcm (Avidity) was co-transformed, and expression was carried out in *Escherichia coli* BL21(DE3), as described previously³³. After collection, cells were lysed by sonication, and immobilized metal affinity chromatography (IMAC) with a Ni-IDA resin (ABT) was used to enrich the His-tagged protein. After cleaving off the His₆ tag with thrombin (Serva Electrophoresis), another round of IMAC was performed to separate the cleaved protein from the tag. To separate the protein from final impurities and non-biotinylated protein, reversed-phase (RP) HPLC with a Reprosil Gold 200 C18 column (Dr. Maisch) was performed using a water/0.1% TFA–acetonitrile gradient.

ACTR was then dissolved to a concentration of 200 μ M in 100 mM potassium phosphate buffer, pH 7.2 (labeling buffer), under a nitrogen atmosphere. For labeling with the first fluorophore, the protein was mixed with Cy3B maleimide (GE Healthcare) at a molar ratio of 1:0.8 and incubated for 3 h at room temperature. Singly labeled protein was purified using RP-HPLC with a Sunfire C18 column (Waters), as described above. After lyophilization and being re-dissolved in labeling buffer for labeling with the second fluorophore, ACTR was labeled by adding LD650 maleimide²² (Lumidyne Technologies) to protein at a molar ratio of 1:0.8. The doubly labeled protein was first purified using

RP-HPLC on Reprosil Gold 200 column, followed by another round of HPLC with a Sunfire C18 to yield very pure protein. The correct mass of doubly labeled ACTR was confirmed by electrospray ionization mass spectrometry (ESI-MS).

NCBD was co-expressed with ACTR from a pET-47b⁺ vector for better expression yields³⁴. The NCBD construct (with an N-terminal Cys) has an N-terminal His₆ tag that is cleavable with HRV 3C protease: MAH-HHHHSAALEVLFQGPCPNRSISPSALQDLLRTLKSPSSPQQQQVLLNLSKSNPQLMAAFIKQRTAKYVANQPQGMQ. Cell lysis and IMAC were carried out in a similar fashion to ACTR, but instead of thrombin, HRV 3C protease was used to cleave the His₆ tag. ACTR and NCBD were subsequently separated by RP-HPLC on a Reprosil Gold column, followed by a second round of purification with a Sunfire C18 column.

Pro α and H1 expression, purification and labeling

The double-cysteine variant Pro α -E56C D110C³⁵ was expressed in *E. coli* C41 DE3; cells were grown in Terrific Broth with kanamycin and induced using 0.5 mM isopropyl β -D-1-thiogalactopyranoside (IPTG) at an OD₆₀₀ of ~ 0.7 and were further grown overnight at 25 °C. Cell pellets were resuspended in denaturing buffer (6 M guanidinium chloride in phosphate-buffered saline (PBS) pH 7.4 with 2 mM dithiothreitol (DTT)); the soluble fraction was collected and applied to a Ni Sepharose excel purification resin (Cytiva) in bulk solution. The resin was washed twice with 5 resin volumes of denaturing buffer including 25 mM imidazole before the extracted sample was applied. The protein was eluted with PBS including 250 or 500 mM imidazole. The protein was dialyzed against 50 mM Tris buffer pH 8, 200 mM NaCl, 2 mM DTT and 1 mM EDTA using a 3.5-kDa molecular cut-off membrane. The histidine tag was cleaved during dialysis with HRV 3C protease. The protein was then purified with Ni Sepharose excel resin again to remove the cleaved tag, and the flow-through was concentrated using a 3-kDa molecular weight cut-off ultrafiltration device (Vivaspin 20, VIVAproducts). The protein was further purified by ion-exchange chromatography using a HiPrep Q FF column (Cytiva). The column was equilibrated with 50 mM Tris buffer pH 7.4, 200 mM NaCl and 2 mM DTT, and after loading the protein on the column, Pro α was eluted in 50 Tris pH 7.4 with a gradient from 200 mM to 1 M NaCl. Fractions containing the purified protein were collected and concentrated before being buffer-exchanged using a HiTrap Desalting column (Cytiva) against freshly prepared and degassed labeling buffer with 100 mM potassium phosphate at pH 7. The eluted protein was labeled by incubating it with Alexa Fluor 488 maleimide at a dye-to-protein molar ratio of 0.7:1 for 1 h at room temperature and then with Alexa Fluor 594 maleimide at a dye-to-protein molar ratio of 1.5:1 overnight at 4 °C. Finally, the labeled protein was separated from free dye on a HiTrap desalting column and then purified further by RP-HPLC on a SunFire C18 column (Waters Corporation) with an elution gradient from 20% acetonitrile and 0.1% trifluoroacetic acid in aqueous solution to 37% acetonitrile. Pro α -containing fractions were lyophilized and resuspended in 10 mM Tris buffer with 200 mM KCl and 1 mM EDTA (pH 7.4) and stored at -80 °C. Unlabeled recombinant wild-type human histone H1.0 was purchased from New England Biolabs (cat. no. M2501S, Ipswich).

Single-molecule FRET measurements

Single-molecule FRET measurements of ACTR and NCBD were performed on a custom-built confocal instrument. Excitation light at 532 nm from a continuous-wave solid-state laser (Laser Boxx, Oxxius) was coupled into the microscope objective (UPlanApo 60x/1.20 W, Olympus) via a triple-band dichroic mirror (z405/530/630, Chroma) at the power of 100 μ W (measured at the back aperture of the objective). Fluorescence and scattered light were collected by the same objective, focused onto a 100- μ m pinhole and separated with a polarizing beam splitter and two dichroic mirrors (HC560, HC662, Semrock). The separated signals were additionally filtered by a neutral density filter (ND1.0, Thorlabs) for the scattered light, bandpass filters for the donor

channels (ET585/65, Chroma) and longpass filters for the acceptor channels (LP647 Chroma), and were focused onto five single-photon avalanche detectors (SPCM-AQR-13, PerkinElmer Optoelectronics). Photon arrival times were recorded by five channels of a HydraHarp 400 counting module (PicoQuant). For fluorescence intensity imaging, the objective was mounted on a combination of two piezo scanners, a P-733.2CL for XY positioning and a PIFOC for Z-positioning (Physik Instrumente). The SymPhoTime 64 software package (PicoQuant) was used for data acquisition.

For ACTR–NCBD measurements, the buffer used for the aqueous phase was 50 mM sodium phosphate containing 0.01% (wt/vol) Tween 20 (Surfact-Amps 20, Thermo Fisher Scientific) and 140 mM β -mercaptoethanol (Sigma-Aldrich) for photoprotection. The initial concentration of ACTR (labeled with Cy3B or LD650) applied to the peripheral inlet as shown in Fig. 2b was 150 pM; 150 nM, 300 nM or 450 nM of unlabeled NCBD was applied to the center inlet, which gave final concentrations of 50 pM ACTR, and 50 nM, 100 nM and 150 nM NCBD, respectively, in the droplets at flow rates of 20 nL min⁻¹ for ACTR, NCBD, and buffer, and 10.4 μ L min⁻¹ for oil. To achieve 25 nM and 75 nM concentrations of NCBD in the droplets, the dilution ratios of the buffer and NCBD (150 nM, 450 nM) inlets were altered to 30 nL min⁻¹ and 10 nL min⁻¹, respectively. Before each set of kinetic data was acquired, droplet formation and flow conditions were checked with the bright-field microscope $\times 4$ objective and high-speed camera mentioned above. After 20 min of flushing and system stabilization, the microfluidic chip was moved to the confocal microscope for single-molecule FRET measurement without stopping the flow. The laser focus was positioned in the center of the channel and the bottom PDMS layer was bleached for 2 min to reduce the fluorescence background. Binding kinetics were acquired by recording fluorescence and scattered light for 10 min (corresponding to at least 21,000 droplets) at each position selected along the observation channel.

Single-molecule FRET measurements of H1–ProT α were performed with a MicroTime 200 confocal microscope (PicoQuant) equipped with a 488 nm diode laser (Sapphire 488–100 CDRH, Coherent) and an Olympus UPlanApo 60 \times /1.20 W objective. To increase brightness, the 488-nm diode laser was set to an average power of 300 μ W and operated in continuous-wave mode. After passing through a 150- μ m pinhole, sample fluorescence was separated into donor and acceptor emission using a dichroic mirror (585DCXR, Chroma). After passing appropriate bandpass filters (Chroma ET525/50M, HQ650/100), each component was focused onto an avalanche photodiode (SPCM-AQR-15, PerkinElmer Optoelectronics, Vaudreuil), and the arrival time of every detected photon was recorded (HydraHarp 400, PicoQuant). For fluorescence intensity imaging, the objective was mounted on a combination of two piezo scanners, a P-733.2CL for XY positioning and a PIFOC for Z positioning (Physik Instrumente). The SymPhoTime 64 software package (PicoQuant) was used for data acquisition.

For H1–ProT α measurements, the buffer used for the aqueous phase was 10 mM Tris-buffered saline (TBS, Carl Roth), with the ionic strength adjusted to 200 mM using KCl (Sigma-Aldrich), 140 mM β -mercaptoethanol (Sigma-Aldrich) for photoprotection and 0.01% Tween 20 (Surfact-Amps 20, Thermo Fisher Scientific) to prevent aggregation. The initial concentration of ProT α (labeled with Alexa Fluor 488 and Alexa Fluor 594) applied to the peripheral inlet, as shown in Fig. 2f, was 150 pM. Unlabeled H1 at 21 nM, 30 nM and 60 nM was delivered from the center inlet channel, the shortest inlet before droplet formation, to minimize adsorption to the channel surface. The final concentrations were 50 pM ProT α , and 7 nM, 10 nM and 20 nM H1, respectively, in the droplets, at flow rates of 20 nL min⁻¹ for ProT α , H1, and buffer, and 10.4 μ L min⁻¹ for oil. Concentrations of 3.5 nM, 15 nM and 30 nM H1 in the droplets were achieved by altering the dilution ratios of buffer and H1 (21 nM, 60 nM) but keeping the total flow rate constant. Following the same procedures as for ACTR–NCBD, the droplet formation and flow conditions were checked

with bright-field illumination and the high-speed camera, after which the microfluidic chip was moved to the confocal microscope for single-molecule FRET measurements without stopping the flow. The laser focus was positioned in the center of the channel, and the bottom PDMS layer was bleached for 2 min to reduce background fluorescence. Binding kinetics were acquired by recording the fluorescence signal for 6 min at each position (corresponding to at least 14,000 droplets) along the observation channel. With 488-nm excitation, the higher background fluorescence of the oil phase containing 1% fluorosurfactant compared with 532-nm excitation could not be bleached sufficiently prior to use (Extended Data Fig. 6c). However, the different fluorescence signals of the oil phase and the fluorophore-labeled molecules in the water droplets could be used to identify individual droplets (Extended Data Fig. 7) without detecting additional scattered light. Measurements in buffer droplets without labeled protein demonstrate the low background contribution from PDMS and buffer (Extended Data Fig. 6e).

Single-molecule FRET data analysis

In all single-molecule FRET measurements, transfer efficiencies were quantified from all selected photon bursts (at least 3,000 bursts), each originating from an individual molecule passing through the confocal volume, according to $E = n_A / (n_A + n_D)$, where n_D and n_A are the numbers of donor and acceptor photons in each burst, respectively, corrected for background, channel crosstalk, acceptor direct excitation, differences in quantum yields of the dyes, and detection efficiencies³⁶. All data analysis was performed with Fretica, a custom add-on for Mathematica (Wolfram Research) available at <https://schuler.bioc.uzh.ch/programs>.

For the analysis of the ACTR–NCBD association kinetics, photon bursts were identified with a threshold of 40 photons per 200- μ s bin, and photons from consecutive bins were combined into one fluorescence burst. For ProT α –H1, a threshold of 60 photons per bin was used. For both reactions, at least 3,000 bursts were selected, and transfer efficiency histograms from the collected bursts for all times were fitted globally with three populations described by Gaussian peak functions. Positions of the peaks were shared fit parameters, and the peak widths were constrained to the values expected from shot-noise broadening. For each histogram, the fraction of bound labeled species was determined from the fraction of the area of the high-efficiency peak. The datasets for the association reaction at different binding partner concentrations (25, 50, 75, 100 and 150 nM NCBD; 3.5, 7, 10, 15, 20 and 30 nM H1; reactions at different concentrations were measured independently at least twice) were fitted globally with a two-state model assuming pseudo-first-order reaction conditions (datasets using 20 and 30 nM H1 measured in the small-scale device were also included in the global fit). k_{on} and k_{off} were obtained from the fit, and K_D was calculated from k_{on} and k_{off} . Steady-state donor anisotropies of ACTR (Cy3B- or LD650-labeled) in the ACTR–NCBD binding time series from Extended Data Fig. 8 obtained from the identified bursts yielded an average value of 0.15 ± 0.01 , indicating that the rotational factor κ^2 in Förster's theory can be approximated by the average value of 2/3 (ref. 37).

Reporting summary

Further information on research design is available in the Nature Portfolio Reporting Summary linked to this article.

Data availability

Source data are provided with this paper.

Code availability

Fretica, a custom add-on package for Mathematica v.12.3 (Wolfram Research), was used for the analysis of single-molecule fluorescence data and is available at <https://github.com/SchulerLab>.

References

29. Hofmann, H. et al. Single-molecule spectroscopy of protein folding in a chaperonin cage. *Proc. Natl Acad. Sci. USA* **107**, 11793–11798 (2010).
30. Dunlop, P. J. & Stokes, R. H. The diffusion coefficients of sodium and potassium iodides in aqueous solution at 25°¹. *J. Am. Chem. Soc.* **73**, 5456–5457 (1951).
31. Zosel, F., Soranno, A., Buholzer, K. J., Nettels, D. & Schuler, B. Depletion interactions modulate the binding between disordered proteins in crowded environments. *Proc. Natl Acad. Sci. USA* **117**, 13480–13489 (2020).
32. Schilling, J., Schöppe, J. & Plückerthun, A. From DARPins to LoopDARPins: novel LoopDARPin design allows the selection of low picomolar binders in a single round of ribosome display. *J. Mol. Biol.* **426**, 691–721 (2014).
33. Cull, M. G. & Schatz, P. J. in *Methods in Enzymology* Vol. 326, 430–440 (Academic Press, 2000).
34. Soranno, A. et al. Single-molecule spectroscopy reveals polymer effects of disordered proteins in crowded environments. *Proc. Natl Acad. Sci. USA* **111**, 4874–4879 (2014).
35. Müller-Späth, S. et al. Charge interactions can dominate the dimensions of intrinsically disordered proteins. *Proc. Natl Acad. Sci. USA* **107**, 14609–14614 (2010).
36. Holmstrom, E. D. et al. in *Methods in Enzymology* Vol. 611 (ed. Rhoades, E.) 287–325 (Academic Press, 2018).
37. Hellenkamp, B. et al. Precision and accuracy of single-molecule FRET measurements—a multi-laboratory benchmark study. *Nat. Methods* **15**, 669–676 (2018).
38. Hess, D. et al. Exploring mechanism of enzyme catalysis by on-chip transient kinetics coupled with global data analysis and molecular modeling. *Chem* **7**, 1066–1079 (2021).

Acknowledgements

We thank the FIRST-CLA Cleanroom at ETH Zurich for their support in microfabrication and the Functional Genomics Center Zurich for performing mass spectrometry. This work was supported by the Swiss National Science Foundation (B.S., A.dM.), the Forschungskredit of

the University of Zurich (T.Y.), the Novo Nordisk Foundation Challenge program REPIN (no. NNF18OC0033926, B.S.) and the Human Frontier Science Program (B.S.).

Author contributions

T.Y. and B.S. conceived the study. T.Y. performed microfluidic system design, microfabrication and system characterization. T.Y. performed single-molecule experiments with input from K.B. and A.S. X.C. performed mask-free two-photon 3D printing. A.dM. provided microfabrication instrumentation. K.B. and A.S. performed protein sample preparation. D.N. developed single-molecule instrumentation and data analysis software. T.Y. and D.N. developed analysis tools for experimental data. T.Y. analyzed the experimental data, with input from K.B., A.S., B.S. and D.N. B.S. supervised the project. T.Y., D.N. and B.S. wrote the manuscript with contributions from all authors.

Competing interests

The authors declare no competing interests.

Additional information

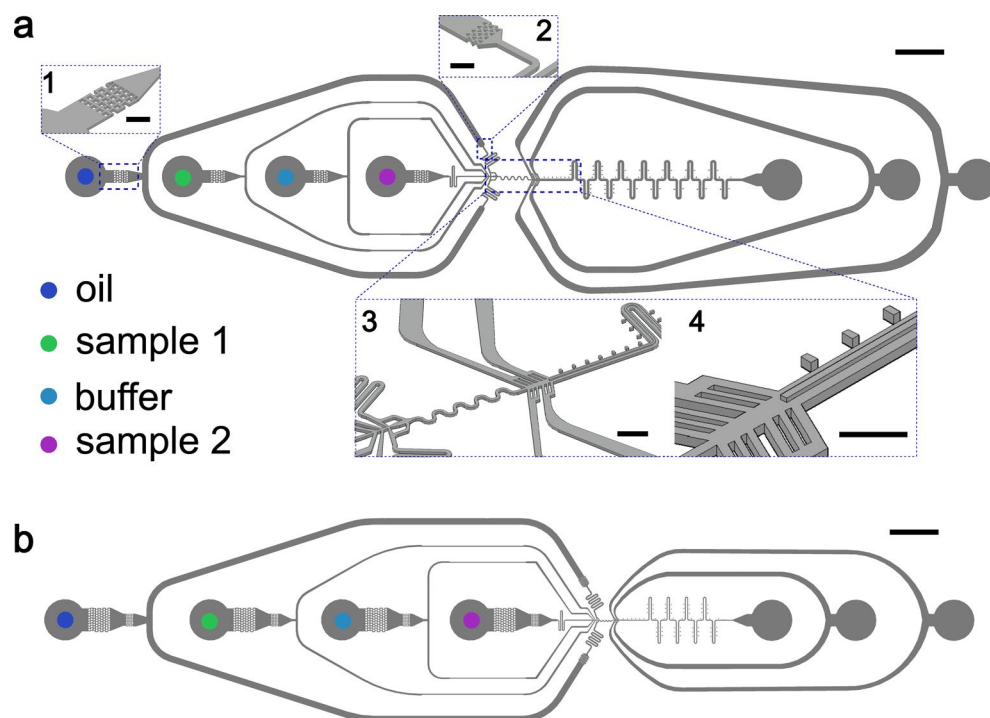
Extended data is available for this paper at <https://doi.org/10.1038/s41592-023-01995-9>.

Supplementary information The online version contains supplementary material available at <https://doi.org/10.1038/s41592-023-01995-9>.

Correspondence and requests for materials should be addressed to Tianjin Yang or Benjamin Schuler.

Peer review information *Nature Methods* thanks the anonymous reviewers for their contribution to the peer review of this work. Peer reviewer reports are available. Primary Handling Editor: Rita Strack, in collaboration with the *Nature Methods* team.

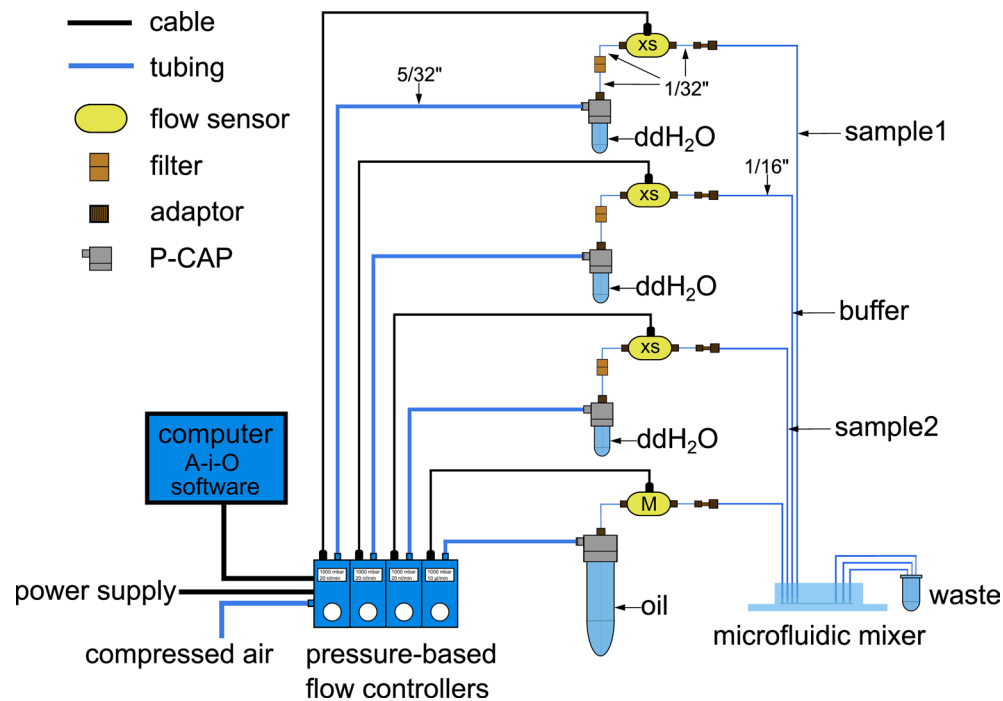
Reprints and permissions information is available at www.nature.com/reprints.



Extended Data Fig. 1 | Designs of the droplet-based microfluidic mixers.

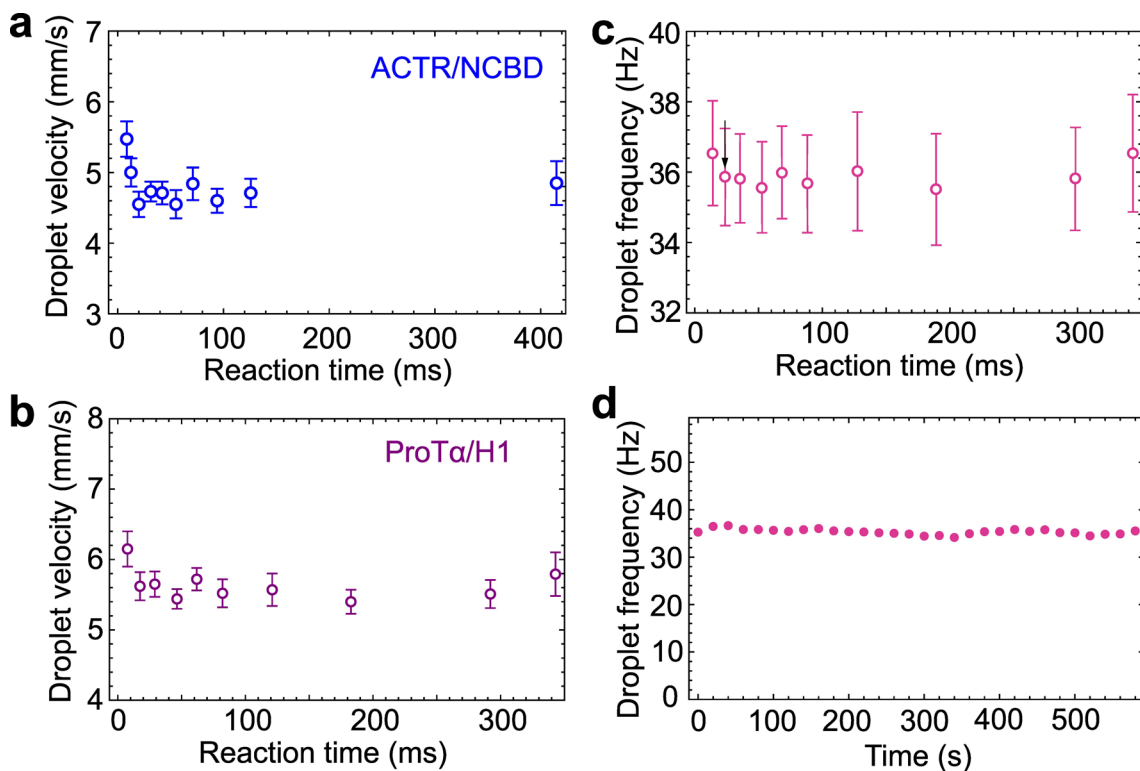
a) Layout of the standard-scale microfluidic mixer, scale bar 1 mm. Oil is used as the carrier phase for the droplets. Three inlets labeled as sample 1, buffer, and sample 2 are used to deliver the aqueous phase to the microfluidic mixer. Right after entering the mixer, all liquids pass microfabricated filters composed of small pillars to avoid dust particles or aggregates entering the channels, as shown in the zooms 1 and 2. The buffer solution sheathing sample 1 allows on-chip dilution and prevents premature mixing with sample 2. Droplets are formed using a flow-focusing geometry (zoom 3), where part of the oil is branched off just before droplet formation and recombined afterwards, which accelerates the droplets directly after formation³⁸. A serpentine channel (zoom 3) follows, which ensures sub-millisecond mixing inside each droplet by chaotic advection. After mixing, most of the oil is drained off via two side channels (zoom 3) to slow down the droplets by two orders of magnitude and allow sufficiently long passage times through the confocal detection volume that enable single-molecule fluorescence detection in the observation channel. A groove at the top of the observation channel (zooms 3, 4) stabilizes the droplets in the

channel center during signal detection to avoid droplet motion perpendicular to the flow direction, especially in the case of varying droplet sizes in different measurements. Markers (zoom 4) were introduced along the observation channel with known spacing to be able to determine the detection position for the position-to-time conversion. The height of the microchannels is 20 μm , the height of the groove is 10 μm , the width of the flow focusing channels is 14 μm , of the observation channel 55 μm , and of the serpentine channel 20 μm . Scale bars in zoom 1, 2, 3, 4: 100 μm . **b)** Layout of the small-scale microfluidic mixer, scale bar: 1 mm. The device follows the same working principle as the standard-scale microfluidic mixer in **a)**, but with scaled-down dimensions of the height (12 μm), the width of the flow focusing channels (6 μm), the observation channel (20 μm), and the serpentine channel (12 μm) to achieve shorter dead times. Double filter arrays are introduced right after the inlets to ensure that no dust particles or aggregates block the small channels. There is no groove structure on top of the observation channel since the droplets fully occupy the channel in this device. More details of the designs can be found in the CAD files provided as supplementary material.



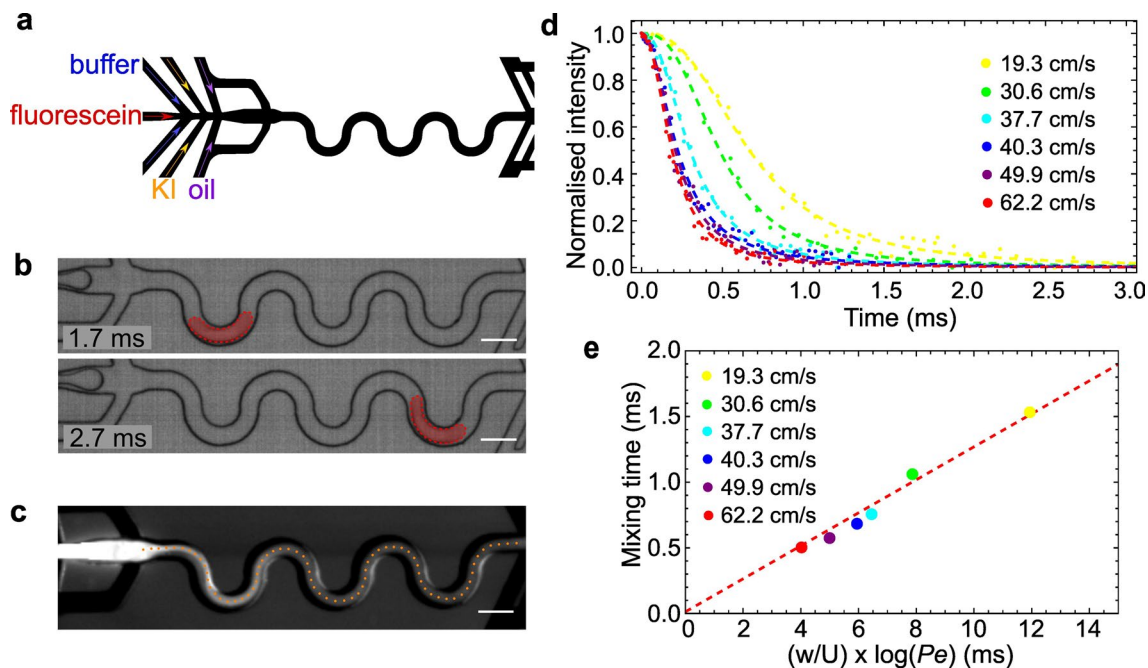
Extended Data Fig. 2 | Fluid control system for the droplet-based microfluidic mixer. Four precision pressure-based flow controllers connected to compressed air were used to provide accurate control of the fluids. Three of the flow controllers were each coupled to an XS flow sensor to accurately monitor the delivery of aqueous phase to sample inlet 1, buffer inlet, and sample inlet 2 with known flow rates for achieving the target concentrations. The three flow controllers delivering aqueous phase were connected via 5/32" OD tubing to a P-CAP sealed on 2-ml Eppendorf tubes containing double-distilled water as reservoirs. 1/32" OD PEEK tubing was used to connect the water reservoirs to the inlets and outlets of the flow sensors with filters inbetween preventing dust particles from clogging the XS flow sensors. Due to a high risk of clogging given the small internal channel diameter (20 μm) of the flow sensor by dust particles,

salt precipitates or biomolecular aggregates, we avoided running sample and buffer solutions through the flow sensor and instead stored sample and buffer solutions in the 1/16" OD PTFE tubing between the flow sensors and the inlets of the microfluidic device. The tubing flow controller was connected via 5/32" OD tubing to the air-tight P-CAP sealed on a 15-ml Falcon tube containing the oil phase delivered to the microfluidic chip. 1/32" OD PEEK tubing was used to connect the oil-phase reservoir to the inlet and outlet of the flow sensors. 1/16" OD PTFE tubing was used to connect the outlet of the flow sensor to the microfluidic oil inlet via an adaptor. The outlets of the microfluidic chip were connected to the waste reservoir via 1/16" OD PTFE tubing. Pressures and flow rates of the four inlets were controlled and recorded during measurements using the Fluigent A-i-o software.

**Extended Data Fig. 3 | Device stability during smFRET measurements.**

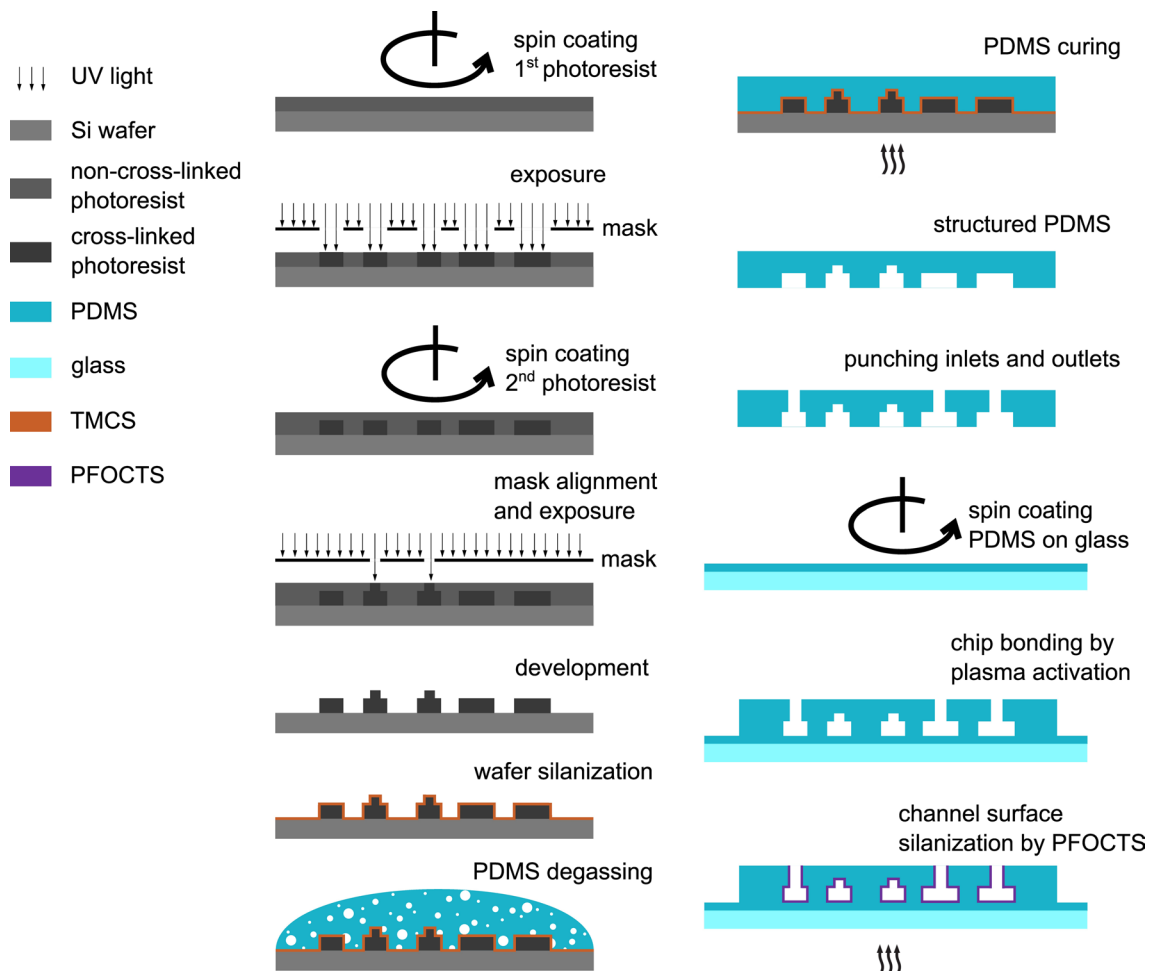
a and **b**) droplet velocities at various reaction times (corresponding to different positions along the observation channel) for measurements with ACTR/NCBD and ProTα/H1, respectively. Signal acquisition at each point was for 10 min, corresponding to between 21,000 and 26000 droplets. Mean values and standard deviations are shown. The total recording time was about three hours. **c**) Droplet frequency at various reaction times from the same data set as in **b**).

The mean and standard deviation are shown as generated from 600 seconds of measurement at each point. The stable droplet velocities and droplet generation frequencies in **a**), **b**), and **c**) demonstrate the long-term stability of the microfluidic mixing device during measurements lasting for hours. **d**) Droplet frequency over time at one representative reaction time (16.2 ms; see arrow in panel **c**) showing the droplet frequency every 20 seconds.



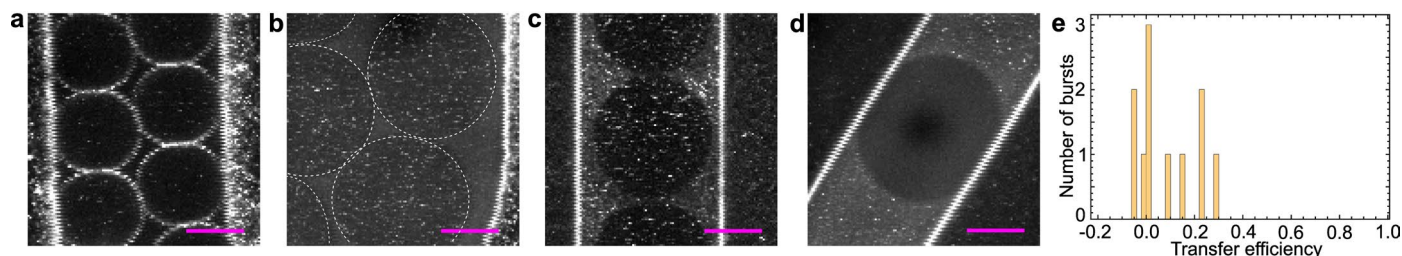
Extended Data Fig. 4 | Quantifying the mixing time via diffusion-limited quenching of fluorescein with potassium iodide (KI). **a** Schematic of the microfluidic channels with the solutions applied to the inlets indicated. **b** Brightfield images taken from a movie recorded at 3000 frames/s for measuring the droplet velocity, U , in the mixing channel, yielding $U=40.3$ cm/s (droplet manually colored for clarity). Scale bar: $40\ \mu\text{m}$. **c** Fluorescence image taken with a 3-second exposure, averaged over 10 consecutive frames showing the decrease of the intensity along the channel due to quenching. At least 1200 droplets were sampled. **d** The fluorescence intensities at different positions along the mixing channel were normalized between 0 and 1 and converted

to the time after the droplets enter the mixing channel. We performed the measurements at a fixed droplet size ($90\ \mu\text{m}$ in the mixing channel) but different velocities from 19.3 to 62.2 cm/s (see legend) and fitted the mixing profiles with Eq. (2). **e** The mixing times (90% of intensity change) were obtained from the fits and plotted as a function of $(w/U) \times \log(Pe)^{16}$, where w is the width of the channel, U is the velocity of the droplet, and $Pe=wU/D$ is the Péclet number, which indicates the ratio of the rate of advection to the rate of diffusion of the fluid. The linear fit of the plot is used as a calibration curve to determine the mixing time based on the velocities of the droplets and the diffusion coefficients of the components in the single-molecule FRET measurements.



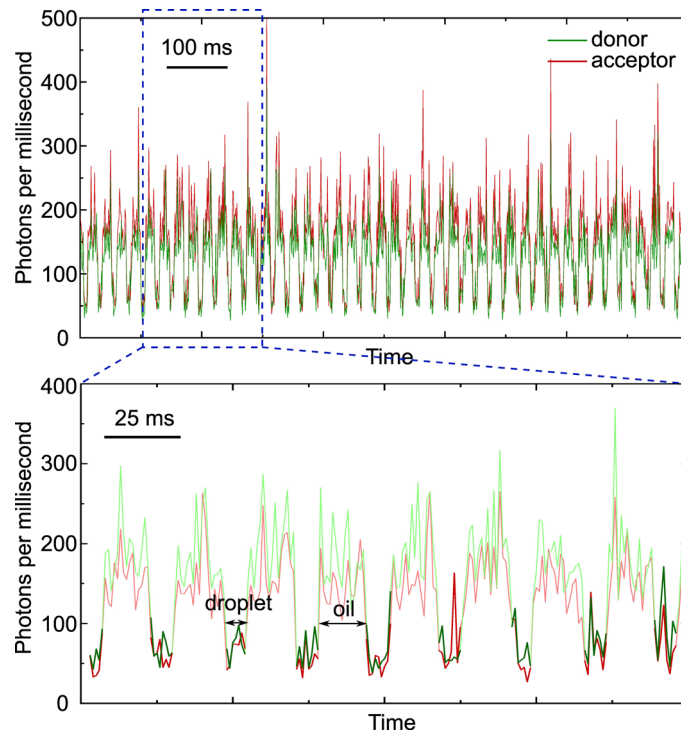
Extended Data Fig. 5 | Microfluidic device fabrication workflow. In the lithography process for master fabrication, SU8-2015 photoresist was deposited on a silicon wafer by spin coating at 2200 rpm to achieve a film thickness of 20 μm . After soft baking (not shown), the wafer was exposed to UV light (energy density: 140 mJ/cm^2 at 365 nm) with the main channel mask aligned above. Then the wafer was placed on a hot plate for 3 minutes at 95 $^\circ\text{C}$ for the post-exposure bake (not shown). Another layer of SU8-2007 was spin-coated on the previous layer at 1500 rpm to achieve a thickness of 10 μm , and was soft-baked for 1 minute at 65 $^\circ\text{C}$, followed by 2 minutes at 95 $^\circ\text{C}$ (not shown). Utilizing the mask aligner, the groove channel photomask was aligned with the exposed structure on the wafer, and another UV exposure (energy density: 120 mJ/cm^2 at 365 nm) was used to create the groove channel. After post-exposure baking for 3 minutes at 95 $^\circ\text{C}$ (not shown), non-crosslinked photoresist was removed by gently shaking the wafer in SU8 developer. Prior to replica molding, the

masters were silanized with TMCS (trimethylchlorosilane) in a desiccator to prevent PDMS adhesion. Microfluidic devices were manufactured using replica molding. A 10:1 wt/wt mixture of PDMS base and curing agent was poured onto the master structure, degassed, and cured in the oven at 70 $^\circ\text{C}$ for 4 h. The cured PDMS structure was peeled off the wafer, cut, and inlet and outlet ports were introduced. A 23 mm \times 30 mm glass cover slide was first cleaned and then spin coated with a thin layer of PDMS (spin coating at 4000 rpm, ~20 μm thickness) as the bottom layer. The structured PDMS device was bonded to the bottom layer after plasma activation. To prevent wetting of the microchannel surfaces by the water phase, and ensure stable and uniformly sized droplets, microfluidic channels were filled with a 5% (by volume) PFOCTS isopropanol solution for 3 min at room temperature right after plasma bonding, then the solution was removed with pressured air, and the device was then placed on a hot plate at 120 $^\circ\text{C}$ for two hours.



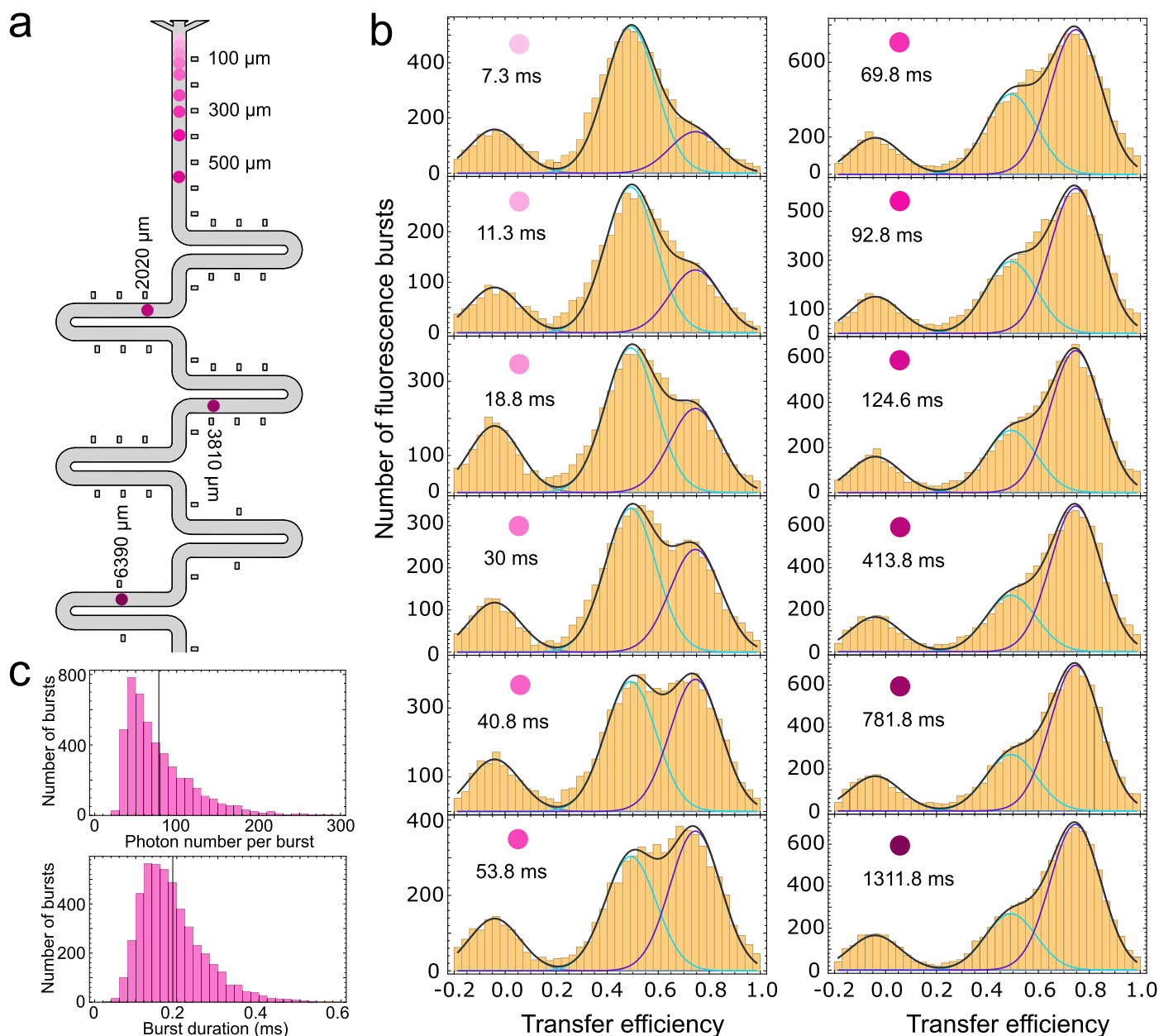
Extended Data Fig. 6 | Fluorescence intensity images of static droplets in the microfluidic channel to monitor surface adhesion. **a)** With too low a PEG-PFPE₂ concentration in the oil phase of 0.25%, surface passivation of the water/oil interface was insufficient, and Cy3B/LD650-labeled ACTR adsorbed to the interface (excitation at 532 nm, detection at 550–610 nm for donor, >647 nm for acceptor). **b)** With the PEG-PFPE₂ concentration increased to 1%, Cy3B/LD650-labeled ACTR did not accumulate at the interfaces (indicated by white dashed lines), but was homogeneously distributed inside the droplets. **c)** Under the same conditions, also no adsorption of Alexa488/594-labeled Prot α -HI to the water/oil interface was observed (excitation at 488 nm, detection at 500–550 nm

for donor, 600–700 nm for acceptor emission). **d)** The oil phase containing 1% PEG-PFPE₂ showed increased fluorescence intensity compared to the droplets containing buffer without sample (excitation at 488 nm). Scale bars: 20 μ m. **e)** Measurement performed in droplets containing buffer but no labeled protein (excitation at 488 nm, detection at 500–550 nm for donor, 600–700 nm for acceptor emission, measured for 15 min, corresponding to 37,185 droplets). The small number of bursts illustrates the low background contribution from PDMS and buffer. Images a), b), c), d), and plot e) are representative experiments from at least 3 independent repeats with similar results.



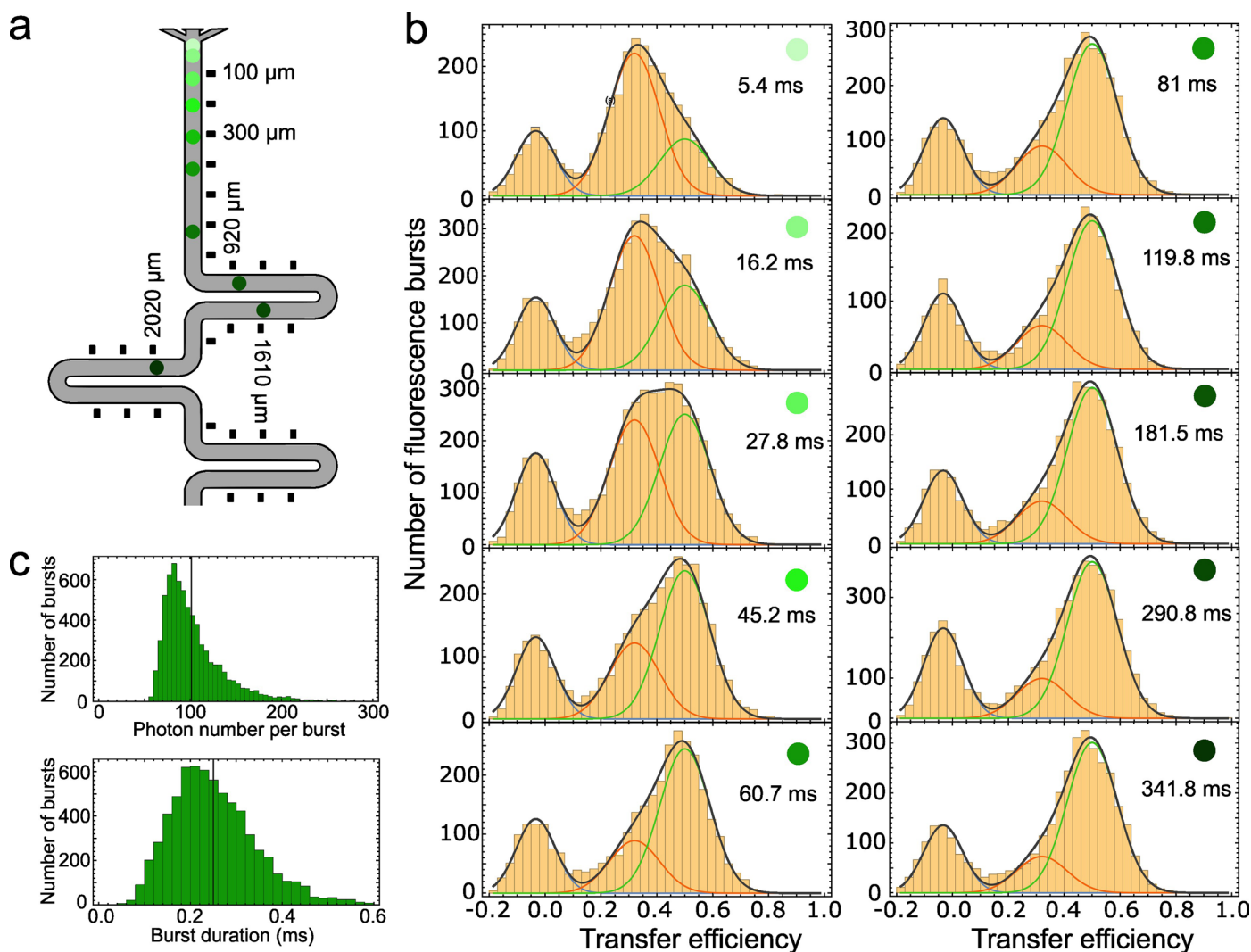
Extended Data Fig. 7 | Time trace of signals from donor and acceptor channels of droplets containing 50 pM Alexa488/594-labeled ProT α -HI complex formed in oil containing 1% (w/w) PEG-PFPE₂. The fluorescence intensity in the oil phase on average exhibits a photon rate of ~ 150 to 200 ms⁻¹,

which is higher than in the droplet phase containing Alexa488/594-labeled ProT α -HI complex (488 nm excitation). The two phases can be identified directly from the donor and acceptor time traces as indicated.



Extended Data Fig. 8 | Series of transfer efficiency histograms of donor- and acceptor-labeled ACTR measured at different times after mixing with unlabeled NCBD. Donor- and acceptor-labeled ACTR (50 pM) was mixed with an excess of unlabeled NCBD (50 nM). **a**) Colored circles indicate the positions along the observation channel at which the measurements were performed. **b**) Histograms measured after mixing, corresponding to the data set shown in Fig. 2c, analyzed with a global fit of all histograms. The low transfer efficiency peak ($\langle E \rangle = 0.51$) corresponds to unbound ACTR, and the high transfer efficiency

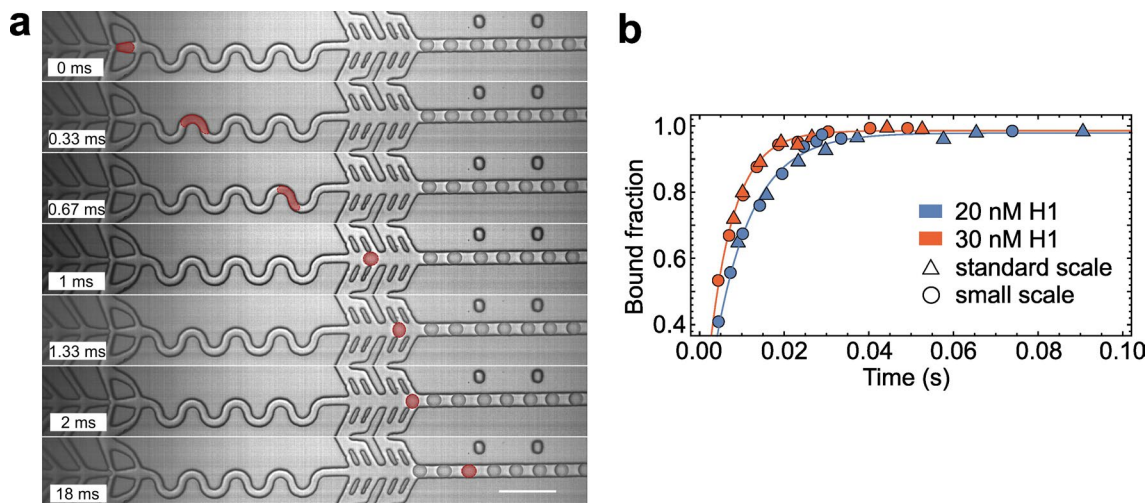
peak ($\langle E \rangle \approx 0.74$) to ACTR bound to NCBD. Over time, the fraction of bound ACTR increases and reaches equilibrium. The peak close to $\langle E \rangle = 0$ originates from molecules without active acceptor dye. Each transfer efficiency histogram was built up from at least 3000 bursts. **c**) Representative histograms of the number of photons per burst and the burst duration from the measurement at 30 ms in **b**). The mean number of photons per burst is 79, and the mean burst duration is 0.19 ms, as indicated by the vertical lines. The total number of bursts is ~7,300, corresponding to ~0.3 bursts per droplet.



Extended Data Fig. 9 | Series of transfer efficiency histograms of donor- and acceptor-labeled ProTx measured at different times after mixing with unlabeled HI. Donor- and acceptor-labeled ProTx (50 pM) was mixed with an excess of unlabeled HI (7 nM). **a**) Colored circles indicate the positions along the observation channel at which the measurements were performed.

b) Histograms measured after mixing, corresponding to the data set shown in Fig. 2h, analyzed with a global fit of all histograms. The low transfer efficiency peak ($\langle E \rangle \approx 0.33$) corresponds to unbound ProTx, and the high transfer efficiency peak ($\langle E \rangle \approx 0.51$) to ProTx bound to HI. Over time, the fraction of bound ProTx increases and reaches equilibrium. The peak close to $\langle E \rangle = 0$ originates from molecules without active acceptor dye. Each transfer efficiency histogram was

built up from at least 3000 bursts. The $\langle E \rangle$ values are within ± 0.03 of the values obtained from equilibrium measurements²⁵. The broadening of the peaks compared to equilibrium measurements is due to the shorter residence time of the molecules as they flow through the confocal volume and the correspondingly lower thresholds for the number of photons used for burst identification. **c**) Representative histograms of the number of photons per burst and the burst duration from the measurement at 81 ms in **b**). The mean number of photons per burst is 102, and the mean burst duration is 0.25 ms, as indicated by the vertical lines. The total number of bursts is -11,200, corresponding to -0.9 bursts per droplet.



Extended Data Fig. 10 | Small-scale microfluidic mixer for reactions with observed rates above -150 s^{-1} . **a)** Snapshots of a manually colored droplet in the small-scale microfluidic mixer indicating the changes of droplet velocity in different regions of the device. Scale bar: $100 \mu\text{m}$. The width of the microfluidic channels is $12 \mu\text{m}$ in the mixing channel, $20 \mu\text{m}$ in the observation channel, and the channel height is $10 \mu\text{m}$. The flow focusing produces smaller droplets than in the standard-scale device that are slightly squeezed as an ellipse with a major axis of $\sim 22 \mu\text{m}$. Under the flow conditions used (oil at $5.8 \mu\text{L}/\text{min}$, ProT α , buffer, and H1 at $10 \text{ nL}/\text{min}$), the dead time before a droplet enters the observation channel is reduced to $1.7 \pm 0.3 \text{ ms}$. The length of the observation

channel is 8.7 mm , corresponding to an observation time window of 1.4 s . The representative snapshots are based on at least 10 independent repeats with similar results. **b)** Comparison of kinetics measured with the standard-scale microfluidic mixing device (triangles) and the small-scale mixing device (circles). ProT α /H1 association kinetics with high concentrations of H1 were measured on both devices. The concentration of ProT α was 50 pM , the concentration of H1 20 nM (blue) and 30 nM (orange) at 200 mM ionic strength. Note the shorter times accessible with the small-scale device. The agreement between the measurements in both devices supports the robustness of the results.

Reporting Summary

Nature Portfolio wishes to improve the reproducibility of the work that we publish. This form provides structure for consistency and transparency in reporting. For further information on Nature Portfolio policies, see our [Editorial Policies](#) and the [Editorial Policy Checklist](#).

Statistics

For all statistical analyses, confirm that the following items are present in the figure legend, table legend, main text, or Methods section.

n/a Confirmed

- The exact sample size (n) for each experimental group/condition, given as a discrete number and unit of measurement
- A statement on whether measurements were taken from distinct samples or whether the same sample was measured repeatedly
- The statistical test(s) used AND whether they are one- or two-sided
Only common tests should be described solely by name; describe more complex techniques in the Methods section.
- A description of all covariates tested
- A description of any assumptions or corrections, such as tests of normality and adjustment for multiple comparisons
- A full description of the statistical parameters including central tendency (e.g. means) or other basic estimates (e.g. regression coefficient) AND variation (e.g. standard deviation) or associated estimates of uncertainty (e.g. confidence intervals)
- For null hypothesis testing, the test statistic (e.g. F , t , r) with confidence intervals, effect sizes, degrees of freedom and P value noted
Give P values as exact values whenever suitable.
- For Bayesian analysis, information on the choice of priors and Markov chain Monte Carlo settings
- For hierarchical and complex designs, identification of the appropriate level for tests and full reporting of outcomes
- Estimates of effect sizes (e.g. Cohen's d , Pearson's r), indicating how they were calculated

Our web collection on [statistics for biologists](#) contains articles on many of the points above.

Software and code

Policy information about [availability of computer code](#)

Data collection SymPhoTime 64 (PicoQuant) was used for single-molecule data collection. Fluigent A-i-O software (Fluigent) was used to record flow rates of the samples delivered to the microfluidic mixer.

Data analysis Fretica, a custom add-on package for Mathematica v.12.3 (Wolfram Research) was used for the analysis of single-molecule fluorescence data and is available at <https://github.com/SchulerLab>. ImageJ (1.52f, National Institutes of Health, USA) was used for image processing.

For manuscripts utilizing custom algorithms or software that are central to the research but not yet described in published literature, software must be made available to editors and reviewers. We strongly encourage code deposition in a community repository (e.g. GitHub). See the Nature Portfolio [guidelines for submitting code & software](#) for further information.

Data

Policy information about [availability of data](#)

All manuscripts must include a [data availability statement](#). This statement should provide the following information, where applicable:

- Accession codes, unique identifiers, or web links for publicly available datasets
- A description of any restrictions on data availability
- For clinical datasets or third party data, please ensure that the statement adheres to our [policy](#)

Source data are provided with this paper.

Human research participants

Policy information about [studies involving human research participants and Sex and Gender in Research](#).

Reporting on sex and gender	n/a
Population characteristics	n/a
Recruitment	n/a
Ethics oversight	n/a

Note that full information on the approval of the study protocol must also be provided in the manuscript.

Field-specific reporting

Please select the one below that is the best fit for your research. If you are not sure, read the appropriate sections before making your selection.

Life sciences Behavioural & social sciences Ecological, evolutionary & environmental sciences

For a reference copy of the document with all sections, see [nature.com/documents/nr-reporting-summary-flat.pdf](https://www.nature.com/documents/nr-reporting-summary-flat.pdf)

Life sciences study design

All studies must disclose on these points even when the disclosure is negative.

Sample size	Statistical methods were not used to determine sample sizes. Sample sizes were determined by the normal throughput of the instrumentation while ensuring that three or more independent replicates were performed for statistical analysis. For single molecule FRET experiments, each replicate reflects approximately more than 3,000 freely diffusing molecules involved. The sample size was found to satisfactorily describe the conformational distribution in the ensemble.
Data exclusions	Bursts arising from molecules with only a single fluorophore and signal from the oil phase were excluded from the analysis as described in Methods.
Replication	All main results were successfully reproduced using different samples, and measured on different days in fresh buffers. The number of experimental replicates are specified in the legends of all figures.
Randomization	This study did not allocate experimental groups thus no randomization was required for the reported experiments.
Blinding	Blinding was not performed. No a priori knowledge could be assumed about the present observations and blinding is therefore not applicable. Data was analyzed systematically as described in the manuscript.

Reporting for specific materials, systems and methods

We require information from authors about some types of materials, experimental systems and methods used in many studies. Here, indicate whether each material, system or method listed is relevant to your study. If you are not sure if a list item applies to your research, read the appropriate section before selecting a response.

Materials & experimental systems

n/a	Involvement in the study
<input checked="" type="checkbox"/>	<input type="checkbox"/> Antibodies
<input checked="" type="checkbox"/>	<input type="checkbox"/> Eukaryotic cell lines
<input checked="" type="checkbox"/>	<input type="checkbox"/> Palaeontology and archaeology
<input checked="" type="checkbox"/>	<input type="checkbox"/> Animals and other organisms
<input checked="" type="checkbox"/>	<input type="checkbox"/> Clinical data
<input checked="" type="checkbox"/>	<input type="checkbox"/> Dual use research of concern

Methods

n/a	Involvement in the study
<input checked="" type="checkbox"/>	<input type="checkbox"/> ChIP-seq
<input checked="" type="checkbox"/>	<input type="checkbox"/> Flow cytometry
<input checked="" type="checkbox"/>	<input type="checkbox"/> MRI-based neuroimaging